MULTISCALE MODELING FOR CRYSTALLINE MATERIALS: A COMPREHENSIVE STUDY IN STATICS AND DYNAMICS

by

Elaine Gorom-Alexander

A dissertation submitted to the faculty of
The University of North Carolina at Charlotte
in partial fulfillment of the requirements
for the degree of Doctor of Philosophy in
Applied Mathematics

Charlotte

2024

Approved by:

_____
Dr. Xingjie Helen Li

_____
Dr. Loc Nguyen

_____
Dr. Duan Chen

_____
Dr. Xiuxia Du

ABSTRACT

ELAINE GOROM-ALEXANDER. Multiscale Modeling for Crystalline Materials: A Comprehensive Study in Statics and Dynamics. (Under the direction of DR. XINGJIE HELEN LI)

Computational materials science plays a crucial role in advancing new and improved materials. To leverage the advantages of local and nonlocal methods and aid in the advancement of predictive capabilities for materials, multiscale models have been introduced. Many such methods have been proposed to overcome computational challenges in accuracy and efficiency. In this work, I begin by presenting a review of some multiscale methods for crystalline modeling to provide context for this dissertation.

Together with my advisor Dr. Xingjie Helen Li, we explore the static behavior of a bottom-up nonlocal-to-local coupling method, Atomistic-to-Continuum coupling, and explore the dynamic behavior of a nonlocal method, Peridynamics, to explore a bimaterial interface.

Inspired by the blending method developed by [1] for nonlocal-to-local coupling, we create a symmetric and consistent blended force-based Atomistic-to-Continuum (AtC) scheme for one-dimensional atomistic chains. AtC coupling schemes have been introduced to utilize the accuracy of atomistic models near known defects and the computational efficiency of continuum models elsewhere. The conditions for the well-posedness of the underlying model are established by analyzing an optimal blending size and blending type to ensure the stability of the H^1 seminorm for the blended force-based operator. We present several numerical experiments to test and confirm the theoretical findings.

Then, we create a Peridynamics-to-Peridynamics scheme to model a bimaterial bar in one dimension. Peridynamics (PD) naturally allows for the simulation of crack propagation in its model due to its use of integro-differentials and time

derivatives instead of the spatial derivatives typical of classical models. Although PD can be computationally intensive, its ability to accurately model fracture behavior, especially at material interfaces, makes it a valuable tool for achieving high accuracy in simulations, especially due to the susceptibility of fracture where differing materials meet. We prove the conservation laws, derive the dispersion relation, and estimate the coefficient of reflection near the interface for this nonlocal-to-nonlocal problem. We seek an optimal nonlocal interaction kernel in the governing equation for the cross-material interaction to reduce spurious artifacts when the kernel is assumed to be constant.

Lastly, I discuss potential future development in Atomistic-to-Continuum coupling and Peridynamics.

DEDICATION

To my family–the Goroms, the Alexanders, and the Ganders.

ACKNOWLEDGEMENTS

I extend my deepest gratitude to my advisor, Dr. Xingjie Helen Li, whose unwavering support, invaluable guidance, and constructive feedback have profoundly influenced my academic journey. Dr. Li's mentorship has been instrumental in my growth as a researcher and scholar. Her insightful ideas have inspired the research presented in this dissertation. I am also grateful for her kindness and intelligence, which have set a high standard for academic mentorship. Her continuous input and feedback have been invaluable in shaping the progression of this work.

Thank you to my committee members, Dr. Loc Nguyen and Dr. Duan Chen, for their guidance throughout my doctoral studies. Special thanks to Dr. Duan Chen, Dr. Loc Nguyen, Dr. Will Brian, and Dr. Shaozhong Deng for their support in providing recommendation letters to support summer internships and job applications. I also thank Dr. Mohammad Kazemi, Dr. Loc Nguyen, Dr. Arindam Roy and Dr. Oleg Safronov for allowing me to join them at soccer games during my first year. This time of reprieve from academic endeavors was very special to me.

I would like to acknowledge The Graduate School and the Department of Mathematics & Statistics for their financial assistance through GASP. Additionally, I appreciate the support from Dr. Xingjie Helen Li's Faculty Early Career Development award from the NSF (NSF-DMS 1847770), which allowed me to focus on growing as a researcher.

I am grateful to Dr. Xingjie Helen Li, Julie Williams-Stogner, and Dr. Terrance Pendleton for their mentoring and guidance in my professional life. Our unique conversations have been invaluable in shaping my personal and professional growth, and I am indebted to them for their support.

There are also many friends and family who have earned my gratitude. Travis, your unwavering support and endless pep talks have meant the world to me. Thank you to my family, Paul, Regina, Kevin, and Steven Gorom, who have pushed

me in all aspects of my life, laughed with me along the way, and helped me reach this milestone. Thank you to my newer family, Brenda, Casey, and Chase Alexander, for accepting me as one of your own and providing unbelievable support. Lastly, a huge thank you to my greatest friends–Logan Spacek and Miranda Cornille. Your friendship, laughter, and conversations have uplifted and carried me.

Finally, I thank all the teachers who inspired me on my journey. I hope to be one of you someday.

TABLE OF CONTENTS

LIST OF TABLES

LIST OF FIGURES

LIST OF SYMBOLS

$(\cdot)^{lin}$ linearized equation

$< \cdot, \cdot >$ inner product

E energy equation

F^{ext} external force

$F_{\ell,k}$ force equation at atom ℓ with k^{th} neighbor interaction

$F_{\ell,}$ force equation at atom ℓ with the summation of all neighbor interaction

$(\cdot)^{a}$ atomistic equation

$(\cdot)^{bqcf}$ force-based blended quasicontinuum equation

$(\cdot)^{c}$ continuum equation

$:=$ defined as

α parameter in the Morse Potential

α transmitted coefficient

β blending function

β reflection coefficient

δ horizon of Peridynamics model for the reference point x

$\frac{\delta}{\delta u_\ell}$ first order variation evaluated at u_ℓ

$\frac{\partial}{\partial t}$ partial derivative in terms of t

$\frac{d}{dx}$ derivative evaluated at x

γ nonlocal interaction kernel

γ_* nonlocal interaction kernel for cross-material interaction

γ_1 nonlocal interaction kernel for material 1

γ_2 nonlocal interaction kernel for material 2

$\|\cdot\|_{\ell_2(\Omega^b)}$ 2-norm evaluated on the blending region Ω_b

$\|\cdot\|_{\ell_2}$ ℓ_2-norm

$\|\cdot\|_{\ell_\infty}$ ∞ -norm

Ω whole domain

ω angular frequency

Ω^a atomistic domain

Ω^b blending domain

Ω^c continuum domain

ϕ atomistic interaction potential per unit cell

ρ mass density

a lattice spacing constant

b external force density

$F_{,k}$ force equation with k^{th} neighbor interaction with the summation of all atoms

K elasticity constant for a material

k wave number

L number of atoms within the blending region Ω_b

M half number of atoms in the atomistic chain

N number of neighbors within the interaction range

u displacement vector

u_ℓ displacement at ℓ

y_ℓ deformation at ℓ

AtC Atomistic-to-Continuum coupling

FEM Finite Element Method

PD Peridynamics

PD-PD Peridynamics-to-Peridynamics model

PDE Partial Differential Equation

subscript e.g., $_x$, $_{xx}$ first derivative, second derivative, etc. for the continuous case

superscript e.g., $^{'}$, $^{''}$ first order backward finite difference, second order central finite difference, etc. for the discrete case

XFEM Extended Finite Element Method

CHAPTER 1: INTRODUCTION

A range of vital products, from airplanes to nuclear pellets to computer chips, need to withstand a variety of conditions to withstand fracture and perform optimally. The study of materials science has now reached a moment when computing technology and mathematical knowledge can lead to even more advances in accurate prediction than ever before [2]. Our fundamental relationship with materials may change radically in a world where the fracture of materials can be predicted with intense accuracy and easily accessible levels of technology.

An important aspect of modeling materials is the ability to reliably predict where material failure will occur. Continuum equations, derived from physical descriptions of materials, are typically characterized by partial differential equations (PDEs). They are typically computationally efficient, utilizing many commonly used finite methods such as finite element, finite volume, mesh-free, spectral, etc. However, they often fail to accurately model material failure because defects lack the regularity required to be captured in this way [2]. Conversely, while atomistic models can be extremely accurate, they are too computationally expensive to be utilized everywhere on a macroscopic material, because of limited computing power. Thus, mesoscopic models were created in an attempt to garner the benefits of both the atomistic and continuum equations, the accuracy of atomistic models with the computational ease of continuum models.

The two main strategies in multiscale models are bottom-up modeling (e.g., [3, 4, 5, 6, 7]) and top-down modeling (e.g., [8, 9, 10, 11, 12, 13, 14, 15, 16, 17, 18]). Bottom-up modeling typically consists of coarse-graining microscopic descriptions (e.g., atomistic models) of material behavior.Bottom-up methods have the poten-

tial to provide atomistic accuracy near defects and continuum finite element efficiency elsewhere [19]; however, this type of modeling requires prior knowledge of potential fractures to use the benefits appropriately. Atomistic-to-continuum coupling is an attractive type of bottom-up modeling, since they can smoothly transition from atomistic to continuum scales. There are many types of AtC coupling methods, including the Arlequin method, morphing approach, quasinonlocal coupling, etc. Top-down methods typically inform macroscopic models (e.g., continuum equations) with physics gleaned from microscopic scales or refining the resolution of said macroscopic models. They can reproduce simple physical principles. It is typical for top-down models to use integrals or integro-differentials where material points interact through short-range forces. Peridynamics is often used in top-down nonlocal approaches for nonlocal mechanics.

The focus of this dissertation is on the static and dynamic properties of coupling methods in multiscale modeling. This encompasses creating a 1D symmetric and consistent force-based blending method for Atomistic-to-Continuum coupling and providing the numerical analysis to ensure the scheme will provide a solution and creating a model for a one-dimensional bimaterial system using Peridynamics and ensuring that physical properties are preserved and numerical artifacts are reduced. The foundation for stability analysis of Peridynamics lies in the AtC numerical analysis. Thus, my objective is to explore the interconnections between bottom-up methods and top-down methods and to understand how their analyses can benefit one another. Additionally, creating the foundation for the treatment of a bimaterial interface using Peridynamics will provide a basis for future local-to-nonlocal coupling in which two or more materials are present such that the governing equation is created and physical properties explored in this dissertation can be used near the interface and a local model can be used further away.

The remainder of this dissertation is arranged as follows:

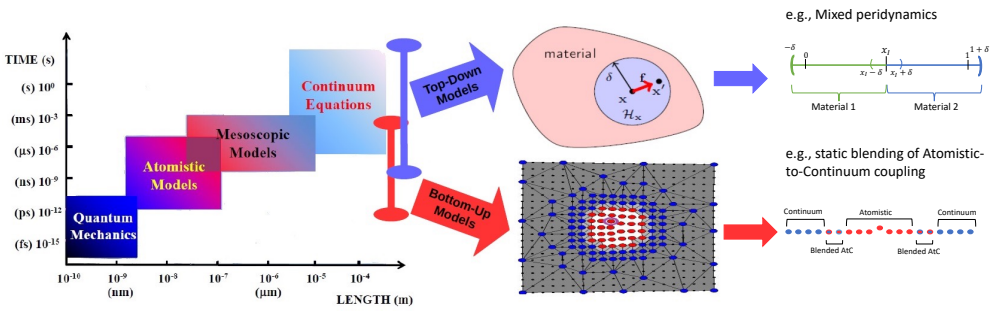

Figure 1.1: This image shows the distinction between the two main strategies in multiscale models and how they relate to the work presented in this dissertation. The time/length scale and the representative AtC and PD images are from Dr. Xingjie Helen Li's notes and the specific 1D images for these projects located on the right were created by me.

- The remainder of Chapter 1 compiles some ideas of the current state of multiscale modeling to give context to this dissertation. The various challenges associated with multiscale modeling are explored.

- Chapter 2 gives a brief background on AtC coupling before delving into the creation of a symmetric, blended force-based AtC coupling scheme and its numerical analysis. Stability parameters are suggested for the convergence of this scheme for several popular iterative methods.

- Chapter 3 delves into the dynamics of a bimaterial system using Peridynamics to model both materials. The accuracy of Peridynamics is crucial in modeling this interface that is susceptible to fracture. We explore the physical consistency of the model and how to reduce spurious reflection.

- Chapter 4 will conclude with possible extensions of the work presented in this dissertation.

1.1 A Review of Local-to-Nonlocal Coupling

Several multiscale methods have been proposed (e.g., [20, 4, 5, 21, 9, 2, 8, 10, 11, 15] and many more). Local-to-nonlocal coupling methods have the potential to

accurately and efficiently reproduce material behavior. Numerous methods and techniques have been suggested to address some of the various computational challenges in fidelity and efficiency. The creation of multiscale modeling schemes and their numerical analyses is a fairly current field, with the first of such methods being created near the end of the twentieth century [22]. Numerical analysis of such schemes remains an open field of research. Fortunately, advances in computing power and parallel computing have increased the use of these methods [2]. The purpose of this dissertation is to add to the field of multiscale models by providing robust numerical analysis to ensure the accuracy and efficiency of the proposed schemes.

In this section, I will briefly discuss a review of some local-to-nonlocal coupling, especially many of those that have informed the work in this dissertation. For a more detailed review of local-to-nonlocal coupling with examples through the lens of nonlocal diffusion and nonlocal mechanics, specifically using Peridynamics for static problems, see [16]. There is limited literature available on the analytical properties and dynamic behavior of local-to-nonlocal coupling.

Some of the challenges in designing a multiscale scheme is ensuring that it is *physically consistent*. A model is physically consistent if it is able to capture the behavior of the system following the underlying physical principles. For a review of many local-to-nonlocal coupling methods and whether or not they are physically consistent, see [16]. In this context, it should be able to capture the phenomenon at various time and length scales.

A model should also be able to accurately behave as expected; and thus, should be *patch-test consistent*. A coupling model is patch-test consistent if, in the absence of external force, the coupled model returns the local solution. For a review of many local-to-nonlocal coupling methods and whether or not they are patch test consistent, see [16]. The main idea behind patch-test consistency is that it can ac-

curately reproduce known solutions.

Also, as a result of combining schemes at various length scales, artifacts can be produced from the model itself. Eliminating or reducing spurious artifacts is also a challenge when designing schemes [16]. In static schemes, the reduction or elimination of "ghost forces" is of import, and, in dynamic schemes, the reduction of artificial reflection can be important to the validity of the proposed scheme.

Treatment of the interface region between coupled schemes is also important and varied among many of the different schemes [16]. Finally, a scheme should be stable and solvable [23].

Many Atomistic-to-Continuum coupling schemes can be categorized as energy-based or force-based. A challenge of many energy-based AtC schemes is the production of "ghost forces". In [24], an energy-based quasicontinuum method is created in which atomistic and Cauchy-Born energy are concurrently coupled. They cannot eliminate the "ghost forces" and thus are not patch-test consistent, but they control the amount of ghost force with the size of the blending region. This approach, which uses the size of the blending region to manage stability and reduce numerical artifacts, is a crucial concept that informs the analysis of our force-based AtC scheme in Chapter 2. Many other energy-based schemes have been proposed that create energy-based schemes that are free from ghost forces [25], [26], [6], [27], but they are beyond the scope of this work.

The force-based blended scheme created in Chapter 2 is inspired by the consistent force-based coupling scheme for Peridynamics and classical elasticity [1]. They introduce a blending function symmetrically that smoothly transitions between the nonlocal and local models such that it passes Newton's third law and is linearly patch-test consistent. Although they do not perform a numerical stability analysis of their scheme, this approach serves as a foundation for extending the force-based scheme developed in this dissertation to provide an optimal blending

width to ensure convergence of the scheme.

Work using Atomistic-to-Continuum coupling and Nonlocal-to-Local methods are an active fields of research. Current work in local-to-nonlocal coupling includes the incorporation of machine learning techniques for ease of parameter selection [28] and its possible use to couple machine learning techniques with Peridynamics [29], [30].

CHAPTER 2: Atomistic-to-Continuum Coupling

2.1 Introduction

This chapter is adapted from the work published in [31]. In this work, we employ a symmetric blending strategy inspired by Seleson et al. for the nonlocal-to-local coupling [10, 11] and develop a new force-based atomistic-to-continuum model for a one-dimensional atomistic chain.

We then study the stability property of the new coupling scheme in terms of the blending function and its blending size using similar mathematical tools from [32]. We investigate the optimal number of atoms within the blending region to ensure the positive definiteness of the resulting force blending operator under the discrete H^1 seminorm. The results admit a very narrow blending region to maintain coercivity and efficiency when the number of atoms is large. In addition, the stability analysis developed in this work is crucial for the convergence of several popular iterative methods for solving large-force equilibrium systems.

The remaining chapter will be arranged as follows.

- In the remainder of this section, background on AtC coupling is introduced and the notation necessary for this work will be presented.

- In Section 2, we introduce the force-based symmetric blending method for an atomistic chain in one dimension. First, we construct an atomistic linearized force equation and a continuum linearized force equation from the atomistic energy equation. The consistency between these methods is discussed in Proposition 2.2.2. A blending function is then introduced to symmetrically combine these two force-based equations.

- In Section 3, we establish the optimal conditions on the size of the blending region for the blending force operator with respect to the H^1 stability. Theorem 2.3.1 and Theorem 2.3.2 establish these conditions.

- In Section 4, a uniform stretch is applied to compute critical strain errors for various types of blending functions with different blending sizes. Also in Section 4, we test a sine and Gaussian external force on the system to model displacement with our force-based blending method. The displacements produced by the blending methods with sufficient blending size agree with those of fully atomistic models. Furthermore, we compare the impact of the interaction range of the atomistic model and observe that an interaction range potential greater than 2 neighbors does not change the displacement significantly.

2.1.1 Atomistic-to-Continuum Coupling of One-Dimensional Chain

2.1.2 Notations

We consider an atomistic chain in one dimension with finite interaction range up to the N-th nearest neighbor and a total number of $2M$ atoms within the domain Ω. We denote the scaled reference lattice $x_\ell = a\ell$ for $\ell \in \mathbb{Z}$ with fixed reference lattice spacing constant $a := \frac{1}{M}$ such that we can select a reference domain that is fixed to
$\Omega = (-1, 1]$. We assume the interaction range, N, to be fixed. The chain is deformed to a current configuration $y_\ell = x_\ell + u_\ell$.

Figure 2.1: Reference lattice for 1D chain.

The displacement field $u = (u_\ell)_{\ell \in \mathbb{Z}} : \mathbb{Z} \to \mathbb{R}$ is assumed to be $2M$ periodic dis-

crete function and $\mathcal{U}$ denotes the space of all $2M$ periodic displacement functions

$$\mathcal{U} := \{u : u_{\ell+2M} = u_\ell | \ell \in \mathbb{Z}\}.$$

Accordingly, we set the deformation space by

$$\mathcal{Y} := \{y : y_\ell = x_\ell + u_\ell | u \in \mathcal{U}, \ell \in \mathbb{Z}\}.$$

We also define the discrete differentiation operator for simplicity, $u^{'}$, on periodic displacements by

$$u^{'}_\ell := \frac{u_{\ell+1} - u_\ell}{a}.$$

Then we may define the higher-order discrete differentiation $u^{''}$, $u^{(3)}$, and $u^{(4)}$ for ℓ by

$$\begin{cases} u^{''}_\ell := \frac{u'_\ell - u'_{\ell-1}}{a}, \\ u^{(3)}_\ell := \frac{u''_{\ell+1} - u''_\ell}{a}, \\ u^{(4)}_\ell := \frac{u^{(3)}_\ell - u^{(3)}_{\ell-1}}{a}. \end{cases} \tag{2.1.1}$$

Note that each higher-order derivative alternates between forward and backward differencing such that each even-order derivative will have a discrete derivative defined central differencing.

We also employ the discrete H^1 seminorm, $|u|^2_{H^1} = \left\| u^{'} \right\|^2_{\ell_2}$ in the stability analysis. For a displacement $u \in \mathcal{U}$ and its discrete derivatives, we employ the discrete ℓ^2 and ℓ^∞ norms for this periodic setting by

$$\|u\|^2_{\ell^2} := \sum_{\ell=-M+1}^{M} |u_\ell|^2 a, \quad \text{and} \quad \|u\|_{\ell^\infty} := \max_{-M+1 \le \ell \le M} |u_\ell| . \tag{2.1.2}$$

In particular, the associated inner product for ℓ_2 is

$$\langle u, w \rangle := \sum_{\ell=-M+1}^{M} u_\ell w_\ell \, a.$$

Meanwhile, we proceed with defining $\widetilde{u} : \mathbb{R} \to \mathbb{R}$ as a quintic spline interpolation of u such that

$$\begin{aligned} \widetilde{u}(a\ell) &= u_\ell, \\ \widetilde{u}(-Ma) &= \widetilde{u}(Ma), \\ \lim_{t \to (a\ell)^-} \frac{d^\omega \widetilde{u}}{dx^\omega}(t) &= \lim_{t \to (a\ell)^+} \frac{d^\omega \widetilde{u}}{dx^\omega}(t), \quad \omega = 1, \ldots, 4 \end{aligned} \tag{2.1.3}$$

As $\widetilde{u}$ is a continuous function, we can introduce the notation for its derivatives, for instance, $\widetilde{u}_x$ as its first derivative at $(a\ell)$, and $\widetilde{u}_{xx}$ as its second derivative at $(a\ell)$, etc.

We can compare the derivatives of $\widetilde{u}(x)$ with the differencing of u_ℓ. Clearly, we have

$$\begin{aligned} u_\ell^{'} &= \widetilde{u}_x(a\ell) + \frac{a}{2}\widetilde{u}_{xx}(\xi) \\ u_\ell^{''} &= \widetilde{u}_{xx}(a\ell) + \frac{a^2}{12}\widetilde{u}_{xxxx}(\tilde{\xi}) \end{aligned} \tag{2.1.4}$$

Note that throughout, the subscript ℓ is used to denote when discrete differentiation is employed; whereas the subscript x is used to denote when considering the true derivatives.

As in [32], we will frequently use the following discrete summation by parts identity:

Lemma 2.1.1. *Suppose $\{u_\ell\}_{\ell=a+1}^{b}$ and $\{v_\ell\}_{\ell=a+1}^{b}$ are two sequences, then we have*

$$\sum_{\ell=a+1}^{b} u_\ell (v_\ell - v_{\ell-1}) = [u_b v_b - u_a v_a] - \sum_{\ell=a+1}^{b} (u_\ell - u_{\ell-1}) v_{\ell-1}.$$

Furthermore, when both $\{u_\ell\}_{\ell=a+1}^{b}$ *and* $\{v_\ell\}_{\ell=a+1}^{b}$ *are periodic sequences with* $u(a) = u(b)$ *and* $v(a) = v(b)$*, we have*

$$\sum_{\ell=a+1}^{b} u_\ell(v_\ell - v_{\ell-1}) = -\sum_{\ell=a+1}^{b} (u_\ell - u_{\ell-1})v_{\ell-1}.$$

We use this lemma to find conditions on coupling to ensure the positive-definiteness of the bilinear form of the symmetric, blended force-based operator.

We state a discrete Poincaré inequality for use in the numerical analysis

$$\|u\|_{\ell^\infty} \leq \|Du\|_{\ell^1} \qquad \forall u \in U.$$

2.2 Derivation of the Symmetric and Consistent Force-Based Scheme

In this section, we will introduce the reference atomistic model and then derive the continuum approximation. After this, we introduce a blending function to symmetrically combine these two models. Utilizing this blending function, we created a coupling scheme for the blended atomistic and continuum forces.

2.2.1 Atomistic and Continuum models

2.2.1.1 Atomistic and Continuum Energy Formulations

We now consider a one-dimensional atomistic periodic chain deformed into configuration $y \in \mathcal{Y}$. Recall that the atomistic periodicity is fixed at $2M$, and the interaction range is fixed to N neighbors. The total atomistic energy for this periodic chain is given by

$$E^{a,tot}(y) := \sum_{\ell=-M+1}^{M} \sum_{\substack{k=-N,\\ k\neq 0}}^{N} \frac{a}{2}\phi\Big(\frac{y_{\ell+k} - y_\ell}{a}\Big), \tag{2.2.1}$$

where $\phi(\cdot) : \mathbb{R} \to \mathbb{R}$ is a Lennard-Jones type inter-atomic potential describing the potential energy between atoms. It can also be viewed as the energy density

per unit volume for pairwise interactions. We assume that $\phi(\cdot)$ has the following properties:

- $\phi(r) = \phi(|r|)$;
- ϕ is at least four times differentiable; and
- $\phi_{xx}(1) > 0$ and $\phi_{xx}(k) \leq 0$ for $k \geq 2$.

In numerical experiments, we utilize the Morse Potential,

$$\phi(r) = D_e \times [1 - e^{-\alpha(r-r_e)}]^2, \tag{2.2.2}$$

for the interaction potential due to its popularity in applications. For a description of the relationship between the Lennard-Jones potential and the Morse potential, see [33]. A graphical illustration can be found in Figure 2.2.

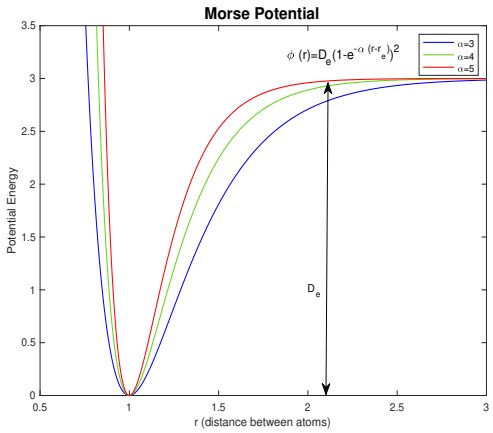

Figure 2.2: Graphical illustration of the Lennard-Jones type interaction potential (Morse potential) used in numerical experiments. Notice that the local minimum is achieved at the nearest neighbour distance $r = r_e$.

Next, we derive the continuum model only by using the first neighbor distance, that is, we only use the differencing u'_ℓ as we approximate the argument for ϕ.

For $k = 2, \ldots, N$, we have

$$\begin{aligned}\frac{y_{\ell+k} - y_\ell}{a} &= \frac{x_{\ell+k} - x_\ell + u_{\ell+k} - u_\ell}{a} \\ &= k + u'_\ell + \sum_{j=1}^{k-1} u'_{\ell+j},\end{aligned}$$

Using the error estimates listed in (2.1.4), we can replace $u'_{\ell+j}$ by u'_ℓ and estimate the discrepancy

$$\begin{aligned}\frac{y_{\ell+k} - y_\ell}{a} &= k + u'_\ell + \sum_{j=1}^{k-1} \widetilde{u}_x \left(a(\ell + j)\right) + c_1 a \\ &= k + u'_\ell + \sum_{j=1}^{k-1} \widetilde{u}_x \left((a\ell)\right) + c_2 a \\ &= k + k u'_\ell + c_3 a,\end{aligned} \tag{2.2.3}$$

where c_1, c_2 and c_3 are constants depending on k and regularity of $\widetilde{u}$. For $k = -N, \ldots, -2$, we can obtain similar consistency estimates.

The atomistic energy equation is rooted in discrete, nonlocal energy descriptions. Assuming the finest mesh with each atom regarded as a node and substituting the previous approximation into the atomistic energy (2.2.1), we thus define the continuum energy as

$$E^c(u) := \sum_{\ell=-M+1}^{M} \sum_{\substack{k=-N, \\ k\neq 0}}^{N} \frac{a}{2} \phi(k + k u'_\ell). \tag{2.2.4}$$

So far, both the atomistic energy and the continuum energy are non-linearly dependent on the displacement field $\{u_\ell\}_{\ell=-M+1}^{M}$, and we would like to apply further simplifications to obtain linear models.

To linearize the total atomistic energy, we follow a similar argument as deriving

the continuum energy,

$$\begin{aligned}\frac{y_{\ell+k}-y_\ell}{a} &= \frac{x_{\ell+k}-x_\ell+u_{\ell+k}-u_\ell}{a}\\ &= k+\frac{u_{\ell+k}-u_\ell}{a}.\end{aligned}$$

Therefore, the total atomistic energy can be written as

$$\begin{aligned}E^{a,tot}(y) &:= \sum_{\ell=-M+1}^{M}\sum_{\substack{k=-N,\\ k\neq 0}}^{N}\frac{a}{2}\phi\Big(\frac{y_{\ell+k}-y_\ell}{a}\Big)\\ &= \sum_{\ell=-M+1}^{M}\sum_{\substack{k=-N,\\ k\neq 0}}^{N}\frac{a}{2}\phi\Big(k+\frac{u_{\ell+k}-u_\ell}{a}\Big)\end{aligned} \tag{2.2.5}$$

Next, we utilize the Taylor expansion to $\phi\Big(k+\frac{u_{\ell+k}-u_\ell}{a}\Big)$ at the reference configuration to linearize the expression.

$$\begin{aligned}\phi(k+\frac{u_{\ell+k}-u_\ell}{a}) = \phi(k)+\frac{u_{\ell+k}-u_\ell}{a}\phi_x(k)+\frac{1}{2}(\frac{u_{\ell+k}-u_\ell}{a})^2\phi_{xx}(k)]\\ +O\left((\frac{u_{\ell+k}-u_\ell}{a})^3\right).\end{aligned}$$

Inserting the Taylor approximation into the atomistic energy equation (2.2.5), we obtain the following result

$$\begin{aligned}\sum_{\ell=-M+1}^{M}\sum_{\substack{k=-N,\\ k\neq 0}}^{N}\frac{a}{2}\Bigg[\phi(k)+\frac{u_{\ell+k}-u_\ell}{a}\phi_x(k)+\frac{1}{2}(\frac{u_{\ell+k}-u_\ell}{a})^2\phi_{xx}(k)\\ +O\left((\frac{u_{\ell+k}-u_\ell}{a})^3\right)\Bigg].\end{aligned} \tag{2.2.6}$$

Then, without loss of generality, we assume $\sum_{\substack{k=-N,\\ k\neq 0}}^{N}\phi(k)=0$ since this term will not contribute to the force. Also, since the reference configuration is a local mini-

mizer and the potential is symmetric, we have

$$\sum_{\substack{k=-N,\\ k\neq 0}}^{N} \frac{u_{\ell+k}-u_\ell}{a}\phi_x(k) = 0.$$

Thus, the linearized atomistic energy is

$$E^{a,lin}(u) := \sum_{\ell=-M+1}^{M} \sum_{\substack{k=-N,\\ k\neq 0}}^{N} \frac{a}{2}\left(\frac{1}{2}\left(\frac{u_{\ell+k}-u_\ell}{a}\right)^2 \phi_{xx}(k)\right). \tag{2.2.7}$$

Following the linearization of the atomistic energy, for the continuum energy, we utilize Taylor expansion to $\phi(k+ku_\ell^{'})$ at the reference configuration to linearize the expression

$$\phi(k+ku_\ell^{'}) = \phi(k) + ku_\ell^{'}\phi_x(k) + \frac{1}{2}(ku_\ell^{'})^2\phi_{xx}(k) + O\left((ku_\ell^{\prime})^3\right).$$

Inserting the Taylor approximation into the continuum energy equation (2.2.4), we obtain the following result

$$\sum_{\ell=-M+1}^{M} \sum_{\substack{k=-N,\\ k\neq 0}}^{N} \frac{a}{2}\left(\phi(k) + ku_\ell^{'}\phi_x(k) + \frac{1}{2}\left(ku_\ell^{'}\right)^2\phi_{xx}(k) + O\left((ku_\ell^{\prime})^3\right)\right). \tag{2.2.8}$$

Following the same justification as above regarding the terms of the Taylor expansion, the linearized continuum energy associated with the finest mesh is defined

as

$$\begin{aligned} E^{c,lin}(u) &:= \sum_{\ell=-M+1}^{M} \sum_{\substack{k=-N, \\ k\neq 0}}^{N} \frac{a}{2}\left(\frac{k^2}{2}(u_\ell')^2\phi_{xx}(k)\right) \\ &= \sum_{\ell=-M+1}^{M}\left(\sum_{k=1}^{N}\frac{k^2}{2}\phi_{xx}(k)\right)(u_\ell')^2 a. \end{aligned} \tag{2.2.9}$$

Remark 2.2.1. Notice that the classical continuum mechanics for interaction range up to the N-th nearest neighbor has the following form:

$$\widetilde{E}^{c,lin}(\widetilde{u}) = \int W\left(\frac{d\widetilde{u}}{dx}\right)^2 dx \tag{2.2.10}$$

where $\frac{d\widetilde{u}}{dx}$ is the deformation field and W represents the strain energy density

$$W := \sum_{k=1}^{N}\frac{k^2}{2}\phi_{xx}(k). \tag{2.2.11}$$

If we use a fine mesh and applying a Riemann sum to approximate the integral of (2.2.10), we can convert (2.2.10) into (2.2.9). Therefore, the linearized continuum energy for a discrete lattice system that was derived from the discrete total atomistic energy is consistent with the theory of classical continuum mechanics. For consistency between classical continuum mechanics and linearized continuum energy, we refer to Appendix A as it closely follows the consistency for the linearized continuum force equation and the description of the atomistic force.

Since we have obtained the atomistic and continuum energies, we will summarize the truncation errors in the next proposition.

Proposition 2.2.1 (Consistency Analysis of Linearized Energy Formulations)**.** *Given a fully refined continuum mesh on the one-dimensional atomistic chain, we derive the lin-*

earized continuum energy equation (2.2.9),

$$E^{c,lin}(u) := \sum_{\ell=-M+1}^{M} \sum_{\substack{k=-N,\\ k\neq 0}}^{N} \frac{a}{2}\left(\frac{k^2}{2}(u_\ell')^2\phi_{xx}(k)\right).$$

from the atomistic energy description, (2.2.1),

$$E^{a,lin}(u) := \sum_{\ell=-M+1}^{M} \sum_{\substack{k=-N,\\ k\neq 0}}^{N} \frac{a}{2}\left(\frac{1}{2}(\frac{u_{\ell+k}-u_\ell}{a})^2\phi_{xx}(k)\right).$$

with the deformed configuration and the displacement field linked by $y_\ell = x_\ell + u_\ell$. Then, the consistency between the linearized continuum energy equation and the atomistic energy equation is $O(a^2)$.

Proof. Comparing $E^{c,lin}$ and $E^{a,lin}$, we have

$$\begin{aligned} E^{c,lin} - E^{a,lin} = &\sum_{\ell=-M+1}^{M} \sum_{\substack{k=-N,\\ k\neq 0}}^{N} \frac{a}{2}\left(\frac{k^2}{2}(u_\ell')^2\phi_{xx}(k)\right) \\ &- \sum_{\ell=-M+1}^{M} \sum_{\substack{k=-N,\\ k\neq 0}}^{N} \frac{a}{2}\left(\frac{1}{2}(\frac{u_{\ell+k}-u_\ell}{a})^2\phi_{xx}(k)\right). \end{aligned}$$

For any $k = 2, ..., N$, we compare $u_{\ell+k}$ around ℓ. Recall the quintic spline interpolation $\widetilde{u}$ defined in (2.1.3), we have

$$u_{\ell+k} = u_\ell + ka\widetilde{u}_x + O(a^2).$$

Thus, for all k,

$$u_{\ell+k} - u_\ell = ka\widetilde{u}_x + O(a^2).$$

Then, the consistency analysis of energies yields:

$$
\begin{aligned}
&E^{c,lin} - E^{a,lin} \\
&\quad = \sum_{\ell=-M+1}^{M} \sum_{\substack{k=-N, \\ k\neq 0}}^{N} \frac{a}{2} \left(\frac{k^2}{2} (u'_\ell)^2 \phi_{xx}(k) \right) \\
&\qquad - \sum_{\ell=-M+1}^{M} \sum_{\substack{k=-N, \\ k\neq 0}}^{N} \frac{a}{2} \left(\frac{1}{2} (\frac{u_{\ell+k} - u_\ell}{a})^2 \phi_{xx}(k) \right) \\
&\quad = \sum_{\ell=-M+1}^{M} \sum_{\substack{k=-N, \\ k\neq 0}}^{N} \frac{a}{2} \left(\frac{k^2}{2} (\frac{u_{\ell+1} - u_\ell}{a})^2 \phi_{xx}(k) \right) \\
&\qquad - \sum_{\ell=-M+1}^{M} \sum_{\substack{k=-N, \\ k\neq 0}}^{N} \frac{a}{2} \left(\frac{1}{2} (\frac{u_{\ell+k} - u_\ell}{a})^2 \phi_{xx}(k) \right) \\
&\quad = \sum_{\ell=-M+1}^{M} \sum_{\substack{k=-N, \\ k\neq 0}}^{N} \frac{a}{2} \left(\frac{k^2}{2} (\frac{a\widetilde{u}_x + O(a^2)}{a})^2 \phi_{xx}(k) \right) \\
&\qquad - \sum_{\ell=-M+1}^{M} \sum_{\substack{k=-N, \\ k\neq 0}}^{N} \frac{a}{2} \left(\frac{1}{2} (\frac{ka\widetilde{u}_x + O(a^2)}{a})^2 \phi_{xx}(k) \right) \\
&\quad = \sum_{\ell=-M+1}^{M} \sum_{\substack{k=-N, \\ k\neq 0}}^{N} \frac{a}{2} \frac{k^2}{2} \phi_{xx}(k) + O(a^2) - \sum_{\ell=-M+1}^{M} \sum_{\substack{k=-N, \\ k\neq 0}}^{N} \frac{a}{2} \frac{k^2}{2} \phi_{xx}(k) + O(a^2) \\
&\quad = O(a^2).
\end{aligned}
$$

□

2.2.1.2 Atomistic and Continuum Force Formulations

Next, we derive the formulae of forces for both linear atomistic and continuum models. Because the mesh is fully refined, the linearized continuum force of atom ℓ can be obtained from taking the first order variation of the linearized continuum

energy (2.2.9) with respect to u_ℓ, we thus get:

$$\begin{aligned} F^{c,lin}_{\ell,}(u) &:= \frac{1}{a}\frac{\delta E^{c,lin}(u)}{\delta u_\ell} = \frac{\delta\left[\sum_{j=-M+1}^{M}\left(\sum_{k=1}^{N}\frac{k^2}{2}\phi_{xx}(k)\right)\left(u_j^{'}\right)^2\right]}{\delta u_\ell} \\ &= -\left(\left(\sum_{k=1}^{N}\frac{k^2}{2}\phi_{xx}(k)\right)\frac{2(u_{\ell+1}-u_\ell)}{a^2} - \left(\sum_{k=1}^{N}\frac{k^2}{2}\phi_{xx}(k)\right)\frac{2(u_\ell-u_{\ell-1})}{a^2}\right) \\ &= -\left(\sum_{k=1}^{N}k^2\phi_{xx}(k)\right)u_\ell^{''}, \end{aligned} \tag{2.2.12}$$

where we recall the shorthand notation $u_\ell^{''}$ as

$$u_\ell^{''} := \frac{u_{\ell+1}-2u_\ell+u_{\ell-1}}{a^2}.$$

For the atomistic forces, we recall $y_\ell = x_\ell + u_\ell$, take the first order variation of the total atomistic energy (2.2.1) at atom ℓ and notice that we employ the forward finite-differencing, hence, we obtain

$$\begin{aligned} F^{a}_{\ell,}(u) &:= \frac{\delta E^{a,tot}}{\delta u_\ell} = \frac{\delta}{\delta u_\ell}\sum_{j=-M+1}^{M}\sum_{\substack{k=-N,\\ k\neq 0}}^{N}\frac{1}{2}\phi(\frac{y_{j+k}-y_j}{a}) \\ &= -\sum_{\substack{k=-N,\\ k\neq 0}}^{N}\frac{1}{2a}\left(\phi_x(k+\frac{u_{\ell+k}-u_\ell}{a}) - \phi_x(k+\frac{u_\ell-u_{\ell-k}}{a})\right). \end{aligned} \tag{2.2.13}$$

Linearizing the forces around the reference configuration by applying the Taylor expansion to $\phi_x(\cdot)$, we obtain the linearized atomistic forces

$$
\begin{aligned}
F^{a,lin}_{\ell,}(u) &:= -\sum_{\substack{k=-N,\\ k\neq 0}}^{N} \frac{1}{2}\phi_{xx}(k)\left(\frac{u_{\ell+k}-2u_{\ell}+u_{\ell-k}}{a^2}\right) \\
&= -\sum_{k=1}^{N} \phi_{xx}(k)\left(\frac{u_{\ell+k}-2u_{\ell}+u_{\ell-k}}{a^2}\right).
\end{aligned}
\tag{2.2.14}
$$

In the next proposition, we summarize the consistency errors between the linearized atomistic and linearized continuum forces.

Proposition 2.2.2 (Consistency analysis of force)**.** *Given a fully refined continuum mesh on the one-dimensional atomistic chain, the linearized atomistic force equation* (2.2.14) *for the atom ℓ is*

$$
F^{a,lin}_{\ell,}(u) := -\sum_{k=1}^{N} \phi_{xx}(k)\left(\frac{u_{\ell+k}-2u_{\ell}+u_{\ell-k}}{a^2}\right)
$$

and the linearized continuum force equation (2.2.12) *for node ℓ is*

$$
F^{c,lin}_{\ell,}(u) = -\left(\sum_{k=1}^{N} k^2\phi_{xx}(k)\right) u''_{\ell}.
$$

Thus, the consistency error between (2.2.14) *and* (2.2.12) *is $O(a^2)$.*

Proof. Comparing $F^{c,lin}$ and $F^{a,lin}$, we have

$$
F^{c,lin}_{\ell,}(u) -_{\ell,} F^{a,lin}(u) = -\sum_{k=1}^{N} \phi_{xx}(k)\left(k^2 u''_{\ell}\right) + \sum_{k=1}^{N} \phi_{xx}(k)\left(\frac{u_{\ell+k}-2u_{\ell}+u_{\ell-k}}{a^2}\right).
$$

For any $k = 2, \ldots, N$, we compare $u_{\ell+k}$ and $u_{\ell-k}$ around ℓ. Recall the quintic-spline

interpolation $\widetilde{u}$ defined in (2.1.3), we have

$$u_{\ell+k} = \widetilde{u}\left(a(\ell+k)\right) - \widetilde{u}\left(a\ell\right) + \widetilde{u}\left(a\ell\right) = u_\ell + ka\widetilde{u}_x + \frac{1}{2}(ka)^2\widetilde{u}_{xx} + \frac{1}{6}(ka)^3\widetilde{u}_{xxx} + O(a^4),$$

$$u_{\ell-k} = \widetilde{u}\left(a(\ell-k)\right) - \widetilde{u}\left(a\ell\right) + \widetilde{u}\left(a\ell\right) = u_\ell - ka\widetilde{u}_x + \frac{1}{2}(ka)^2\widetilde{u}_{xx} - \frac{1}{6}(ka)^3\widetilde{u}_{xxx} + O(a^4).$$

Utilizing this Taylor expansion for the linear atomistic and linear continuum force equations, the consistency analysis yields

$$\begin{aligned}
&F_{\ell,}^{c,lin}(u) - F_{\ell,}^{a,lin}(u) \\
&\quad = -\sum_{k=1}^{N} \phi_{xx}(k)\left(k^2 u_\ell''\right) + \sum_{k=1}^{N} \phi_{xx}(k)\left(\frac{u_{\ell+k} - 2u_\ell + u_{\ell-k}}{a^2}\right) \\
&\quad = -\sum_{k=1}^{N} \phi_{xx}(k)\left(k^2 \frac{u_{\ell+1} - 2u_\ell + u_{\ell-1}}{a^2}\right) + \sum_{k=1}^{N} \phi_{xx}(k)\left(k^2\widetilde{u}_{xx} + O(a^2)\right) \\
&\quad = -\sum_{k=1}^{N} \phi_{xx}(k)\left(k^2\widetilde{u}_{xx} + O(a^2)\right) + \sum_{k=1}^{N} \phi_{xx}(k)\left(k^2\widetilde{u}_{xx} + O(a^2)\right) \\
&\quad = O(a^2).
\end{aligned}$$

A more thorough proof can be seen in Subsection A. □

Remark 2.2.2. Notice that a is chosen to be $\frac{1}{M}$ with M large; therefore, the consistency error becomes small when the number of atoms within Ω is sufficiently large.

2.2.2 Derivation of a Symmetric Blending Model for the AtC Coupling

In this section, we will derive a symmetric and consistent force-based Atomistic-to-Continuum scheme for the one-dimensional atomistic chain.

We first divide the domain of interest into three distinct subdomains:

- Ω^a: the domain described by the atomistic force;

- Ω^c: the domain described by the continuum force; and
- Ω^b: the blending region where the atomistic and continuum force models are both used.

We now introduce a smooth blending function β that can be defined as such:

Definition 2.2.1 (Definition of blending function)**.** We may define a smooth blending function β_ℓ such that:

$$\beta_\ell = \begin{cases} 1, & \ell \in \Omega^a \\ 0, & \ell \in \Omega^c \\ \in (0,1), & \ell \in \Omega^b. \end{cases} \tag{2.2.15}$$

This blending function can take many forms and we will employ linear-spline, cubic-spline, and quintic-spline blending functions as can be seen in the following figure.

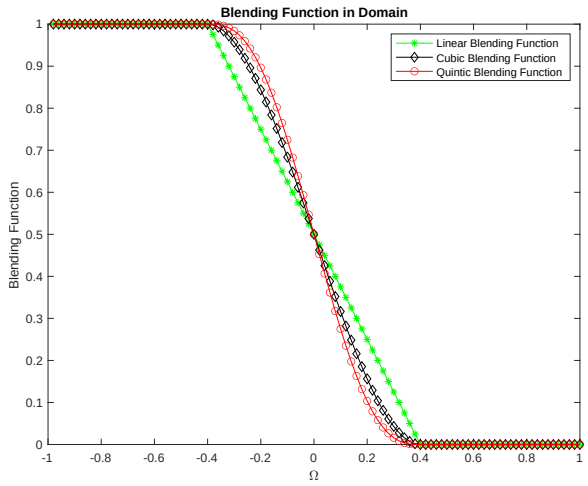

Figure 2.3: Possible blending functions that were included in the numerical simulations.

Notice that creating a linearized force equation will give way to easier analysis in studying the stability of the scheme and providing insights on the coupling

conditions of more general cases, so we focus on blending the linearized atomistic and continuum forces. For a consistent symmetry, we start from $k = -N, \ldots, N$, and $k \neq 0$. Consequently, we start from the linearized, atomistic force equation in (2.2.14) and incorporate the blending function β_ℓ as follows:

$$F_{\ell,}^{a,lin} := -\sum_{k=1}^{N} \phi_{xx}(k) \frac{u_{\ell+k} - 2u_\ell + u_{\ell-k}}{a^2} = -\sum_{\substack{k=-N, \\ k\neq 0}}^{N} \frac{1}{2}\phi_{xx}(k) \frac{u_{\ell+k} - 2u_\ell + u_{\ell-k}}{a^2}$$

$$= -\sum_{\substack{k=-N, \\ k\neq 0}}^{N} \left(\frac{\beta_\ell + \beta_{\ell+k}}{2}\right) \frac{1}{2}\phi_{xx}(k) \frac{u_{\ell+k} - 2u_\ell + u_{\ell-k}}{a^2}$$

$$- \sum_{\substack{k=-N, \\ k\neq 0}}^{N} \left(1 - \frac{\beta_\ell + \beta_{\ell+k}}{2}\right) \frac{1}{2}\phi_{xx}(k) \frac{u_{\ell+k} - 2u_\ell + u_{\ell-k}}{a^2},$$

such that the term $\frac{u_{\ell+|k|} - 2u_\ell + u_{\ell-|k|}}{a^2}$ is multiplied by the pair $\left(\frac{\beta_\ell + \beta_{\ell+|k|}}{2}\right)$ and $\left(\frac{\beta_\ell + \beta_{\ell-|k|}}{2}\right)$, respectively. Next, we further simplify and get

$$F_{\ell,}^{a,lin} = -\sum_{k=1}^{N} \left(\frac{\beta_{\ell-k} + 2\beta_\ell + \beta_{\ell+k}}{4}\right) \phi_{xx}(k) \frac{u_{\ell+k} - 2u_\ell + u_{\ell-k}}{a^2}$$

$$- \sum_{k=1}^{N} \left(1 - \frac{\beta_{\ell-k} + 2\beta_\ell + \beta_{\ell+k}}{4}\right) \phi_{xx}(k) \frac{u_{\ell+k} - 2u_\ell + u_{\ell-k}}{a^2}. \quad (2.2.16)$$

Then, we approximate the second term of the equation by using the linearized continuum portion. Therefore, we get the blended quasicontinuum force function

which is defined as:

$$F_{\ell,}^{bqcf,lin}(u) := -\sum_{k=1}^{N}\left(\frac{\beta_{\ell-k}+2\beta_{\ell}+\beta_{\ell+k}}{4}\right)\phi_{xx}(k)\frac{u_{\ell+k}-2u_{\ell}+u_{\ell-k}}{a^2} - \sum_{k=1}^{N}\left(1-\frac{\beta_{\ell-k}+2\beta_{\ell}+\beta_{\ell+k}}{4}\right)\phi_{xx}(k)k^2\frac{u_{\ell+1}-2u_{\ell}+u_{\ell-1}}{a^2} \tag{2.2.17}$$

$$= -\sum_{k=1}^{N}\left(\frac{\beta_{\ell-k}+2\beta_{\ell}+\beta_{\ell+k}}{4}\right)\phi_{xx}(k)\frac{u_{\ell+k}-2u_{\ell}+u_{\ell-k}}{a^2} - \sum_{k=1}^{N}\left(1-\frac{\beta_{\ell-k}+2\beta_{\ell}+\beta_{\ell+k}}{4}\right)\phi_{xx}(k)k^2u_{\ell}''. \tag{2.2.18}$$

Remark 2.2.3. As $\ell-k$ and $\ell+k$ are both employed in the term of the blending function, this blending operator is symmetric as in [10].

We also see that the first term recovers (2.2.14) for $\beta \equiv 0$, and the second term recovers (2.2.12) for $\beta \equiv 1$. Thus, the consistency error between the linearized $F_{\ell,}^{bqcf,lin}$ and $F_{\ell,}^{a,lin}$ is also of $O(a^2)$.

2.3 Stability Analysis for the Linearized Blending Model

2.3.1 Bilinear Form of Linearized Blending Model

In this section we study the size of the blending region with respect to the H^1 stability of the blending operator following [34] which has advantages over the H^2 stability in that it allows the inclusion of defects in the analysis similar to [35], [36].

This is achieved by obtaining the optimal conditions in which the linearized coupling operator is positive definite under the discrete H^1 semi-norm.

From (2.2.17), we consider the bilinear form

$$\langle F_{,}^{bqcf,lin}(u), v\rangle = \langle F_{,1}^{bqcf,lin}(u), v\rangle + \sum_{k=2}^{N}\langle F_{,k}^{bqcf,lin}(u), v\rangle, \quad \forall v \in \mathcal{U}, \tag{2.3.1}$$

where the first neighbor interaction—the first term—is set apart due to its simplic-

ity in analysis. The second term accounts for the next-nearest neighbor to the N-th nearest neighbor.

To observe the stability of the operator, we first look at the nearest and next-nearest neighbor interaction, for simplicity and for the coercivity assumption on $\phi_{xx}(1) > 0$ and $\phi_{xx}(k) \leq 0$ with $k \geq 2$, to find the constraints on the size of the blending region. Then, we discuss how the next-nearest-neighbor analysis can be extended to the general N-th neighbor interaction.

The discrete stability analysis is inspired by and similar to the analogous continuous analysis for the force-based operator that can be seen in the Appendix B. We proceed with the analysis for the discrete case.

2.3.2 Stability Analysis for Next-Nearest Neighbor Interaction Range: $N = 2$.

Lemma 2.3.1. *For any displacements $u = (u_\ell)_{\ell=-M+1}^{M}$ from the deformed configuration $y_\ell = x_\ell + u_\ell$, the bilinear forms of nearest neighbor and the next-nearest neighbor interaction operator can be written as*

$$\begin{aligned} < F_{,1}^{bqcf,lin}(u), u > &= \phi_{xx}(1)\left\|u'\right\|_{\ell_2}^2 \\ < F_{,2}^{bqcf,lin}(u), u > &= 2\Bigg\{2\phi_{xx}(2)\left\|u'\right\|_{\ell_2}^2 - \frac{\phi_{xx}(2)}{2}a^2\left\|\sqrt{\beta}u''\right\|_{\ell_2}^2 \\ &\qquad + \frac{\phi_{xx}(2)}{2}a^2\left\|\sqrt{|\beta''|}u'\right\|_{\ell_2}^2 + R + S\Bigg\}. \end{aligned} \tag{2.3.2}$$

where

$$R := \sum_{\ell=-M+1}^{M} \frac{\phi_{xx}(2)}{2}\left(u'_\ell \beta^{(3)}_{\ell-1}(u_{\ell-1}) - u''_\ell \beta''_\ell u'_\ell a\right) a^3$$

and

$$S := \sum_{\ell=-M+1}^{M} \frac{\phi_{xx}(2)}{2}(u'_\ell)a^2\left(\beta'_\ell u'_\ell - \beta'_{\ell-2}u'_{\ell-2}\right).$$

Proof. For the nearest-neighbor interaction, as $F^{a,lin}$ and $F^{c,lin}$ coincide, we have

$$\begin{aligned} < F_{,1}^{bqcf,lin}(u), u > &= -\sum_{\ell=-M+1}^{M} \left[\phi_{xx}(1) a \left(\frac{u_{\ell+1} - 2u_\ell + u_{\ell-1}}{a^2} \right) \right] u_\ell \\ &= -\sum_{\ell=-M+1}^{M} \phi_{xx}(1) u_\ell'' u_\ell a. \end{aligned}$$

Then, using the discrete derivative and summation by parts formula from Lemma 2.1.1, we conclude that

$$\begin{aligned} < F_{,1}^{bqcf,lin}(u), u > &= -\sum_{\ell=-M+1}^{M} \phi_{xx}(1) u_\ell'' u_\ell a \\ &= \phi_{xx}(1) \left\| u' \right\|_{\ell_2}^2. \end{aligned}$$

For, the next-nearest neighbor interaction, recall from (2.2.17), the linearized blending operator $F_{\ell,2}^{bqcf,lin}$ is the following

$$\begin{aligned} F_{\ell,2}^{bqcf,lin}(u) = -\Bigg[&\left(\frac{\beta_{\ell+k} + 2\beta_\ell + \beta_{\ell-k}}{4} \right) \phi_{xx}(k) \left(\frac{u_{\ell+k} - 2u_\ell + u_{\ell-k}}{a^2} \right) \\ &+ \left(1 - \frac{\beta_{\ell+k} + 2\beta_\ell + \beta_{\ell-k}}{4} \right) \phi_{xx}(k) \left(\frac{u_{\ell+1} - 2u_\ell + u_{\ell-1}}{a^2} \right) k^2 \Bigg] \Bigg|_{k=2}. \end{aligned}$$

So, we can conclude that the bilinear form with test function u is

$$\begin{aligned} \langle F_{,2}^{bqcf,lin}(u), u \rangle &= \sum_{\ell=-M+1}^{M} F_{\ell,2}^{bqcf,lin}(u) \cdot u_\ell a \\ &= \sum_{\ell=-M+1}^{M} \Bigg\{ -\left(\frac{\beta_{\ell+2} + 2\beta_\ell + \beta_{\ell-2}}{4} \right) \phi_{xx}(2) \left(\frac{u_{\ell+2} - 2u_\ell + u_{\ell-2}}{a^2} \right) a \\ &\quad - \left(1 - \frac{\beta_{\ell+2} + 2\beta_\ell + \beta_{\ell-2}}{4} \right) \phi_{xx}(2) \left(\frac{u_{\ell+1} - 2u_\ell + u_{\ell-1}}{a^2} \right) 4a \Bigg\} \cdot u_\ell. \end{aligned} \tag{2.3.3}$$

We particularly focus on terms contributed to β_ℓ as the other terms could be similarly treated. Hence, we divide the constant '1' in (2.3.3) by $1 = \frac{1}{4} + \frac{2}{4} + \frac{1}{4}$, collect

the terms contributed to β_ℓ and recall the finite difference defined in (2.1.1), then we have

$$
\begin{aligned}
T :=& \frac{-\phi_{xx}(2)}{2}\left[\sum_{\ell=-M+1}^{M}\left(\frac{u_{\ell+2}-2u_\ell+u_{\ell-2}}{a}\right)(\beta_\ell u_\ell)\right. && (2.3.4)\\
&\left.+(1-\beta_\ell)\left(\frac{u_{\ell+1}-2u_\ell+u_{\ell-1}}{a}\right)4u_\ell\right]\\
=& \frac{-\phi_{xx}(2)}{2}\left[\sum_{\ell=-M+1}^{M}\left(u_{\ell+1}^{'}+u_\ell^{'}-u_{\ell-1}^{'}-u_{\ell-2}^{'}\right)(\beta_\ell u_\ell)\right. && (2.3.5)\\
&\left.+(1-\beta_\ell)\left(u_\ell^{'}-u_{\ell-1}^{'}\right)4u_\ell\right]\\
=& \frac{-\phi_{xx}(2)}{2}\left[\sum_{\ell=-M+1}^{M}\left(u_\ell^{'}-u_{\ell-1}^{'}\right)4u_\ell\right]\\
&+\frac{-\phi_{xx}(2)}{2}\sum_{\ell=-M+1}^{M}\left[\left(u_{\ell+1}^{'}-u_\ell^{'}\right)-2\left(u_\ell^{'}-u_{\ell-1}^{'}\right)\right. && (2.3.6)\\
&\left.+\left(u_{\ell-1}^{'}-u_{\ell-2}^{'}\right)\right]\cdot\left(\beta_\ell u_\ell\right)\\
=:& T_1+T_2. && (2.3.7)
\end{aligned}
$$

We consider T_1 first by using Lemma 2.1.1

$$
\begin{aligned}
T_1 &= \sum_{\ell=-M+1}^{M}\frac{-\phi_{xx}(2)}{2}\left(u_\ell^{'}-u_{\ell-1}^{'}\right)4u_\ell\\
&= \sum_{\ell=-M+1}^{M}\frac{\phi_{xx}(2)}{2}u_{\ell-1}^{'}4\left(u_\ell-u_{\ell-1}\right)\\
&= \sum_{\ell=-M+1}^{M}\frac{\phi_{xx}(2)}{2}u_{\ell-1}^{'}4\left(u_{\ell-1}^{'}\right)a\\
&= 2\phi_{xx}(2)\|u^{'}\|_{\ell_2}^2.
\end{aligned}
\qquad (2.3.8)
$$

Treatment of T_2 is still mainly based on Lemma 2.1.1. We have

$$
\begin{aligned}
T_2 = & \sum_{\ell=-M+1}^{M} \frac{-\phi_{xx}(2)}{2} \Bigg[\Big(\Big(u'_{\ell+1} - u'_{\ell} \Big) - \Big(u'_{\ell} - u'_{\ell-1} \Big) \Big) - \Bigg(\Big(u'_{\ell} - u'_{\ell-1} \Big) \\
& \qquad - \Big(u'_{\ell-1} - u'_{\ell-2} \Big) \Bigg) \Bigg] \cdot \Big(\beta_\ell u_\ell \Big) \\
= & \sum_{\ell=-M+1}^{M} \frac{\phi_{xx}(2)}{2} \Bigg[\Big(\Big(u'_{\ell+1} - u'_{\ell} \Big) - \Big(u'_{\ell} - u'_{\ell-1} \Big) \Big) \Bigg] \cdot \Big(\beta_{\ell+1} u_{\ell+1} - \beta_\ell u_\ell \Big) \\
= & \sum_{\ell=-M+1}^{M} \frac{\phi_{xx}(2)}{2} \Big(u''_{\ell} - u''_{\ell-1} \Big) a \cdot \Big(\beta_{\ell+1} u_{\ell+1} - \beta_\ell u_\ell \Big) \\
= & \sum_{\ell=-M+1}^{M} \frac{-\phi_{xx}(2)}{2} \Big(u''_{\ell} \Big) a \cdot \Big[\Big(\beta_{\ell+1} u_{\ell+1} - \beta_\ell u_\ell \Big) - \Big(\beta_\ell u_\ell - \beta_{\ell-1} u_{\ell-1} \Big) \Big] \\
= & \sum_{\ell=-M+1}^{M} \frac{-\phi_{xx}(2)}{2} \Big(u''_{\ell} \Big) a \cdot \Bigg[\big(\beta_{\ell+1} u_{\ell+1} - \beta_\ell u_{\ell+1} \big) + \big(\beta_\ell u_{\ell+1} - 2\beta_\ell u_\ell + \beta_\ell u_{\ell-1} \big) \\
& \qquad - \big(\beta_\ell u_{\ell-1} - \beta_{\ell-1} u_{\ell-1} \big) \Bigg] \\
= & \sum_{\ell=-M+1}^{M} \frac{-\phi_{xx}(2)}{2} \Big(u''_{\ell} \Big) \cdot \beta_\ell u''_\ell a^3 + \frac{-\phi_{xx}(2)}{2} \Big(u''_{\ell} \Big) \cdot \Big[\beta'_\ell u_{\ell+1} - \beta'_{\ell-1} u_{\ell-1} \Big] a^2 \\
= & : -\frac{\phi_{xx}(2)}{2} a^2 \| \sqrt{\beta} u'' \|_{\ell_2}^2 + T_{22}.
\end{aligned}
$$

Now we mainly focus on T_{22} term,

$$
\begin{aligned}
T_{22} = & \sum_{\ell=-M+1}^{M} \frac{-\phi_{xx}(2)}{2} \Big(u'_{\ell} - u'_{\ell-1} \Big) \cdot \Big[\beta'_\ell u_{\ell+1} - \beta'_{\ell-1} u_{\ell-1} \Big] a \\
= & \sum_{\ell=-M+1}^{M} \frac{\phi_{xx}(2)}{2} \Big(u'_{\ell} \Big) \cdot \Big[\Big(\beta'_\ell u_{\ell+1} - \beta'_{\ell-1} u_{\ell-1} \Big) - \Big(\beta'_{\ell-1} u_\ell - \beta'_{\ell-2} u_{\ell-2} \Big) \Big] a.
\end{aligned}
$$

We work on

$$\begin{aligned}
&\left(\beta_\ell^{'} u_{\ell+1} - \beta_{\ell-1}^{'} u_{\ell-1}\right) - \left(\beta_{\ell-1}^{'} u_\ell - \beta_{\ell-2}^{'} u_{\ell-2}\right) \\
&= \beta_\ell^{'}(u_{\ell+1} - u_{\ell-1}) + u_{\ell-1}\left(\beta_\ell^{'} - 2\beta_{\ell-1}^{'} + \beta_{\ell-2}^{'}\right) + \beta_{\ell-1}^{'}(u_{\ell-1} - u_\ell) \\
&\qquad + \beta_{\ell-2}^{'}(u_{\ell-2} - u_{\ell-1}) \\
&= \beta_\ell^{'}(u_\ell' + u_{\ell-1}')a + u_{\ell-1}\beta_{\ell-1}^{(3)}a^2 - \beta_{\ell-1}^{'}u_{\ell-1}'a - \beta_{\ell-2}'u_{\ell-2}'a.
\end{aligned}$$

Then we plug into T_{22} to get

$$\begin{aligned}
T_{22} =& \sum_{\ell=-M+1}^{M} \frac{\phi_{xx}(2)}{2}\left(u_\ell^{'}\right) \cdot \Bigg[\beta_\ell^{'}(u_\ell' + u_{\ell-1}')a + u_{\ell-1}\beta_{\ell-1}^{(3)}a^2 \\
&\qquad - \beta_{\ell-1}^{'}u_{\ell-1}'a - \beta_{\ell-2}'u_{\ell-2}'a\Bigg]a \\
=& \frac{\phi_{xx}(2)}{2} \sum_{\ell=-M+1}^{M}\left(u_\ell'\right)\Bigg(\left[u_{\ell-1}\beta_{\ell-1}^{(3)}a^2 + \left(\beta_\ell' u_{\ell-1}' - \beta_{\ell-1}' u_{\ell-1}'\right)a\right]a + \\
&\qquad \left[\beta_\ell' u_\ell' - \beta_{\ell-2}' u_{\ell-2}'\right]a^2 \\
=& \frac{\phi_{xx}(2)}{2} \sum_{\ell=-M+1}^{M}\left(\left(u_\ell^{'}\right)\beta_{\ell-1}^{(3)}\left(u_{\ell-1}\right) + \left(u_\ell'\right)^2\beta_\ell'' - u_\ell''\beta_\ell''u_\ell' a\right)a^3 \\
&+ \frac{\phi_{xx}(2)}{2} \sum_{\ell=-M+1}^{M}\left(\beta_\ell' u_\ell' - \beta_{\ell-2}' u_{\ell-2}'\right)u_\ell' a^2.
\end{aligned}$$

Summarizing all the terms T_1, T_2, T_{22} for the terms that belong to β_ℓ in (2.3.3) and treating those for $\beta_{\ell-2}$ and $\beta_{\ell+2}$ in a similar way, we get (2.3.2) and R, S terms.

□

Remark 2.3.1. The terms R and S from above are viewed as "residual terms" as in [34]. Thus, we will estimate their bounds controlled by the support of β_ℓ', the size of the blending region, in pursuit of the positive definiteness of the bilinear form.

Lemma 2.3.2. *Let R, S be defined as above, then we have the following estimates*

$$\begin{aligned} |R| &\leq \frac{(-\phi_{xx}(2))}{2}\left(c_3 L^{-\frac{5}{2}}a^{-\frac{1}{2}} + 2c_2(L)^{-2}\right)\left\|u'\right\|_{\ell_2}^2, \\ |S| &\leq \Big(-\phi_{xx}(2)\Big)c_1(L)^{-1}\|u'\|_{\ell_2}^2, \end{aligned} \tag{2.3.9}$$

where L is the number of atoms within the blending region Ω_b, $a = \frac{1}{M}$ being the lattice spacing, and $2M$ being the total number of atoms within the periodic domain $\Omega = (-1, 1]$, and the constants c_1, c_2 and c_3 depend on $\beta^{(j)}$ with $j = 1, \ldots, 3$, respectively.

Proof. Recall that

$$R = \sum_{\ell=-M+1}^{M} \frac{\phi_{xx}(2)}{2}\left(u_\ell' \beta_{\ell-1}^{(3)}(u_{\ell-1}) - u_\ell'' \beta_\ell'' u_\ell' a\right) a^3.$$

Also notice that the finite differences of β are non-zero only on Ω_b, so utilizing the fact that $\phi_{xx}(2) \leq 0$ and Hölder's Inequality, we get

$$\begin{aligned} |R| &\leq \left|\sum_{\ell\in\Omega^b} \frac{\phi_{xx}(2)}{2}(u_\ell')\left(\beta_\ell^{(3)}(u_{\ell-1})\right)a^3\right| + \left|\sum_{\ell\in\Omega^b} \frac{\phi_{xx}(2)}{2} u_\ell'' \beta_\ell'' u_\ell' a^4\right| \\ &\leq \frac{-\phi_{xx}(2)}{2}\left\|\beta^{(3)}\right\|_{\ell^\infty}\left\|u'\right\|_{\ell_2(\Omega^b)}\|u\|_{\ell_2(\Omega^b)}\, a^2 \\ &\quad + \frac{-\phi_{xx}(2)}{2}\|\beta^{(2)}\|_{\ell^\infty}\|u''\|_{\ell_2(\Omega^b)}\,\|u'\|_{\ell_2(\Omega^b)} a^3. \end{aligned}$$

Also note that $|\Omega_b| = La$ and by the discrete Poincaré Inequality, we have

$\|u\|_{\ell_{2(\Omega^b)}} \leq (La)^{\frac{1}{2}} \left\|u^{'}\right\|_{\ell_2}$. Also, we use the fact that $\left\|\beta^{(j)}\right\|_{\ell^\infty} \leq c\,(La)^{-j}$. Then

$$\begin{aligned}
|R| &\leq \frac{-\phi_{xx}(2)}{2}\left\|\beta^{(3)}\right\|_{\ell^\infty}\left\|u^{'}\right\|_{\ell_2(\Omega^b)}\|u\|_{\ell_2(\Omega^b)}\,a^2 \\
&\quad + \frac{-\phi_{xx}(2)}{2}\|\beta^{(2)}\|_{\ell^\infty}\|u''\|_{\ell_2(\Omega^b)}\,\|u'\|_{\ell_2(\Omega^b)}a^3 \\
&\leq \frac{-\phi_{xx}(2)}{2}c_3(La)^{-3}(La)^{\frac{1}{2}}\left\|u^{'}\right\|_{\ell_2}^2\,a^2 + \frac{-\phi_{xx}(2)}{2}c_2(La)^{-2}\frac{2}{a}\|u'\|_{\ell_2}^2 a^3 \\
&\leq \frac{-\phi_{xx}(2)}{2}\left(c_3 L^{-\frac{5}{2}}a^{-\frac{1}{2}} + 2c_2(L)^{-2}\right)\left\|u^{'}\right\|_{\ell_2}^2.
\end{aligned}$$

Next, we bound S. Recall that

$$S := \sum_{\ell=-M+1}^{M} \frac{\phi_{xx}(2)}{2}(u_\ell^{'})a^2\left(\beta_\ell' u_\ell^{'} - \beta_{\ell-2}^{'}u_{\ell-2}^{'}\right).$$

Utilizing similar inequalities, we obtain

$$\begin{aligned}
|S| &\leq \frac{-\phi_{xx}(2)}{2}\|\beta'\|_{\ell^\infty}\cdot 2\|u'\|_{\ell_2}^2 a \\
&\leq \frac{-\phi_{xx}(2)}{2}c_1(La)^{-1}\cdot 2\|u'\|_{\ell_2}^2 a \\
&= \Big(-\phi_{xx}(2)\Big)c_1(L)^{-1}\|u'\|_{\ell_2}^2.
\end{aligned}$$

Hence, we prove the lemma. □

Theorem 2.3.1. *Suppose that the number of atoms M within the chain model is sufficiently large, or equivalently, the lattice spacing $a = \frac{1}{M}$ is sufficiently small; also suppose that the fully atomistic model with next-nearest-neighbor interaction $N = 2$, is stable so that $[\phi_{xx}(1) + 4\phi_{xx}(2)] > 0$. Let L denote the number of atoms within the blending region, and let the blending function β be sufficiently smooth such that $\left\|\beta^{(j)}\right\|_\infty \leq (La)^{-j}$. Then there exists a positive constant $\widetilde{C}$ such that*

$$\sum_{k=1}^{2}\sum_{\ell=-M+1}^{M}\langle F_{\ell,k}^{bqcf,lin}u, u\rangle \geq \widetilde{C}\left\|u^{'}\right\|_{\ell_2}^2 \tag{2.3.10}$$

$\widetilde{C}$ is strictly bounded above zero as $a = \frac{1}{M} \to 0$.

Proof. For $N = 2$ and from Lemma 2.3.1, the blended force-based operator satisfies

$$\begin{aligned}\sum_{\ell=-M+1}^{M} < F_{\ell,2}^{bqcf,lin}(u), u >= \left(\phi_{xx}(1) + 4\phi_{xx}(2)\right)\left\|u^{'}\right\|_{\ell_2}^2 - \phi_{xx}(2)a^2\left\|\sqrt{\beta}u^{''}\right\|_{\ell_2}^2 \\ + \phi_{xx}(2)a^2\left\|\sqrt{\beta^{''}}u^{'}\right\|_{\ell_2}^2 + 2R + 2S.\end{aligned} \tag{2.3.11}$$

From Lemma 2.3.2, we have

$$\begin{aligned}|2R + 2S| &\leq -\frac{\phi_{xx}(2)}{2}\left(2c_3L^{-\frac{5}{2}}a^{-\frac{1}{2}} + 4c_2L^{-2} + c_1L^{-1}\right)\left\|u^{'}\right\|_{\ell_2}^2 \\ &\leq -\frac{\phi_{xx}(2)}{2}\left(c_4L^{-\frac{5}{2}}a^{-\frac{1}{2}}\right)\left\|u^{'}\right\|_{\ell_2}^2,\end{aligned} \tag{2.3.12}$$

hence, we have

$$2R + 2S \geq \frac{\phi_{xx}(2)}{2}\left(c_4L^{-\frac{5}{2}}a^{-\frac{1}{2}}\right)\left\|u^{'}\right\|_{\ell_2}^2$$

with the latter inequality following from $L^{-2} \leq L^{-1} \leq L^{-\frac{5}{2}}a^{-\frac{1}{2}}$ as $L^{-\frac{5}{2}}a^{-\frac{1}{2}}$ dominates the latter two terms when a is sufficiently small.

From (2.3.11), we want to observe the terms that do not favor coercivity in the terms of the H^1 semi-norm. By construction, $\phi_{xx}(1) > 0$. Thus, we focus our attention on the subsequent terms with $\phi_{xx}(2)$. Since $\phi_{xx}(2) \leq 0$, we have

$$-\phi_{xx}(2)a^2\left\|\sqrt{\beta}u^{''}\right\|_{\ell_2}^2 \geq 0,$$

and thus it does not negatively contribute. For the third term we observe that

$$\phi_{xx}(2)a^2\left\|\sqrt{\beta^{''}}u^{'}\right\|_{\ell_2}^2 \geq \phi_{xx}(2)c_5L^{-2}\left\|u^{'}\right\|_{\ell_2}^2$$

because of $\phi_{xx}(2) \leq 0$. For up to $N = 2$ neighbor interaction, we have from the

coercivity of atomistic model that $\phi''(1) + 4\phi''(2) > 0$, hence, for the linearized force-blended model, we have

$$\begin{aligned}\langle F_{,1}^{bqcf,lin} + F_{,2}^{bqcf,lin}, u\rangle &\geq \left[\phi_{xx}(1) + \phi_{xx}(2)\left(4 + c_4 L^{-\frac{5}{2}} a^{-\frac{1}{2}} + c_5 L^{-2}\right)\right] \left\|u'\right\|_{\ell_2}^2 \\ &\geq \widetilde{C}\left\|u'\right\|_{\ell_2}^2\end{aligned}$$

for $\widetilde{C} = \left(\phi_{xx}(1) + 2\phi_{xx}(2)\right) > 0$ strictly positive, independent of $a \to 0$, and if $L^{-\frac{5}{2}} a^{-\frac{1}{2}} \lesssim 1/c_4$ that is $L = \widehat{C} a^{-\frac{1}{5}} = \widehat{C} M^{\frac{1}{5}}$ for some $\widehat{C} > 0$

□

Corollary 2.3.1. *The optimal blending size to ensure the positive definiteness of the linear B-QCF operator with the next-nearest-neighbor interaction, $F_{,}^{bqcf,2lin}$, is* $L = \widehat{C} a^{-\frac{1}{5}} = \widehat{C} M^{\frac{1}{5}}$.

2.3.3 Stability Analysis for general N-th Nearest Neighbor Interaction Range

The work for the next-nearest neighbor interaction is extended to the general N-the nearest neighbor interaction.

Theorem 2.3.2. *Suppose that the number of atoms M is sufficiently large, which is equivalent to $a = \frac{1}{M}$ being sufficiently small, and the blending function β is sufficiently smooth. Also, we assume that the fully atomistic model is stable so that*

$$\left[\phi_{xx}(1) + \sum_{k=1}^{N} k^2 \phi_{xx}(k)\right] > 0.$$

If the blending size L satisfies $L = \widetilde{C} a^{-\frac{1}{5}}$, then the linear B-QCF operator $F_{,}^{bqcf,lin}$ is positive-definite in terms of the H^1 semi-norm

$$\sum_{k=1}^{N} \sum_{\ell=-M+1}^{M} \langle F_{\ell,k}^{bqcf,lin} u, u\rangle \geq \widetilde{C}\left\|u'\right\|_{\ell_2}^2, \tag{2.3.13}$$

where $\widetilde{C}$ is strictly bounded above zero as $a = \frac{1}{M} \to 0$.

Proof. To observe the general form of the N-th neighbor interaction range, we notice that for $k = 3, \dots, N$

$$\begin{aligned}
&\langle F_{,k}^{bqcf,lin}(u), u\rangle \\
&\quad = -\phi_{xx}(k) \sum_{\ell=-M+1}^{M} \Bigg\{ \left(\frac{\beta_{\ell+k} + 2\beta_\ell + \beta_{\ell-k}}{4}\right) \left(\frac{u_{\ell+k} - 2u_\ell + u_{\ell-k}}{a^2}\right) \\
&\qquad + \left(1 - \frac{\beta_{\ell+k} + 2\beta_\ell + \beta_{\ell-k}}{4}\right) k^2 \left(\frac{u_{\ell+1} - 2u_\ell + u_{\ell-1}}{a^2}\right) \Bigg\} u_\ell a.
\end{aligned} \tag{2.3.14}$$

The k-th neighbor interaction differs by having $\beta_{\ell\pm k}$ terms which are treated similarly to β_ℓ terms. $\phi_{xx}(k)$ is a non-positive constant term for all $k \geq 2$.

Similarly to the previous subsection, we fix an interaction range k and at the moment only consider all terms that contribute to β_ℓ, thus we get

$$\begin{aligned}
T :=& -\frac{\phi_{xx}(k)}{2} \sum_{\ell=-M+1}^{M} \left(k^2 \frac{u_{\ell+1} - 2u_\ell + u_{\ell-1}}{a}\right)(u_\ell) \\
&- \frac{\phi_{xx}(k)}{2} \sum_{\ell=-M+1}^{M} \left[\left(\frac{u_{\ell+k} - 2u_\ell + u_{\ell-k}}{a} - k^2 \frac{u_{\ell+1} - 2u_\ell + u_{\ell-1}}{a}\right)\left(\beta_\ell u_\ell\right)\right] \\
=& T_1 + T_2.
\end{aligned}$$

For T_1, we similarly have

$$\begin{aligned}
T_1 &= -\frac{\phi_{xx}(k)}{2} \sum_{\ell=-M+1}^{M} \left(k^2 \frac{u_{\ell+1} - 2u_\ell + u_{\ell-1}}{a}\right)(u_\ell) \\
&= -\frac{\phi_{xx}(k)}{2} \sum_{\ell=-M+1}^{M} k^2 \left(u'_\ell - u'_{\ell-1}\right) u_\ell = \frac{k^2}{2} \phi_{xx}(k) \|u'\|_{\ell_2}^2.
\end{aligned} \tag{2.3.15}$$

For T_2, we have

$$\begin{aligned} T_2 &= -\frac{\phi_{xx}(k)}{2} \sum_{\ell=-M+1}^{M} \left[\left(\frac{u_{\ell+k} - 2u_\ell + u_{\ell-k}}{a} - k^2 \frac{u_{\ell+1} - 2u_\ell + u_{\ell-1}}{a} \right) \left(\beta_\ell u_\ell \right) \right] \\ &= -\frac{\phi_{xx}(k)}{2} \sum_{\ell=-M+1}^{M} \left[\left(\sum_{j=1}^{k} \sum_{s=1}^{k} u''_{\ell-j+s} \right) - k^2 u''_\ell \right] \left(a\beta_\ell u_\ell \right) \\ &= -\frac{\phi_{xx}(k)}{2} \sum_{\ell=-M+1}^{M} \left[\sum_{j=1}^{k} \sum_{s=1}^{k} \left(u''_{\ell-j+s} - u''_\ell \right) \right] \left(a\beta_\ell u_\ell \right). \end{aligned}$$

Due to the exact symmetry of j and s, we have

$$\sum_{j=1}^{k} \sum_{s=1}^{k} u''_{\ell-j+s} = \sum_{j=1}^{k} \sum_{s=1}^{k} u''_{\ell-s+j}.$$

Hence, T_2 can be converted into a symmetrical form

$$\begin{aligned} T_2 &= -\frac{\phi_{xx}(k)}{2} \sum_{\ell=-M+1}^{M} \left[\sum_{j=1}^{k} \sum_{s=1}^{k} \left(u''_{\ell-j+s} - u''_\ell \right) \right] \left(a\beta_\ell u_\ell \right) \\ &= -\frac{\phi_{xx}(k)}{4} \sum_{\ell=-M+1}^{M} \left[\sum_{j=1}^{k} \sum_{s=1}^{k} \left(u''_{\ell-j+s} - 2u''_\ell + u''_{\ell+j-s} \right) \right] \left(a\beta_\ell u_\ell \right) \\ &= -\frac{\phi_{xx}(k)}{4} \sum_{\ell=-M+1}^{M} \left[\sum_{j=1}^{k} \sum_{s=1}^{k} \left(u''_{\ell-j+s} - u''_\ell \right) - \left(u''_\ell - u''_{\ell+j-s} \right) \right] \left(a\beta_\ell u_\ell \right). \end{aligned} \tag{2.3.16}$$

Therefore by the discrete summation by parts formula, we have

$$\begin{aligned}
T_2 =& \frac{\phi_{xx}(k)}{4} \sum_{\ell=-M+1}^{M} \left[\sum_{j=1}^{k} \sum_{s=1}^{k} \left(u''_{\ell-j+s} - u''_{\ell} \right) \right] a \left(\beta_{\ell-j+s} u_{\ell-j+s} - \beta_{\ell} u_{\ell} \right) \\
=& \frac{-\phi_{xx}(k)}{4} \sum_{\ell=-M+1}^{M} \left[\sum_{j=1}^{k} \sum_{s=1}^{k} u''_{\ell} a \right] \left(\left(\beta_{\ell-j+s} u_{\ell-j+s} - \beta_{\ell} u_{\ell} \right) \right. \\
& \qquad \left. - \left(\beta_{\ell} u_{\ell} - \beta_{\ell+j-s} u_{\ell+j-s} \right) \right) \\
=& \frac{-\phi_{xx}(k)}{4} \sum_{\ell=-M+1}^{M} \left[\sum_{j=1}^{k} \sum_{s=1}^{k} u''_{\ell} a \right] \left(\beta_{\ell-j+s} u_{\ell-j+s} - 2\beta_{\ell} u_{\ell} + \beta_{\ell+j-s} u_{\ell+j-s} \right).
\end{aligned} \tag{2.3.17}$$

Then, we simplify the term using its symmetry:

$$\begin{aligned}
\left(\beta_{\ell-j+s} u_{\ell-j+s} - 2\beta_{\ell} u_{\ell} + \beta_{\ell+j-s} u_{\ell+j-s} \right) &\overset{r:=j-s}{=} \left(\beta_{\ell-r} u_{\ell-r} - 2\beta_{\ell} u_{\ell} + \beta_{\ell+r} u_{\ell+r} \right) \\
&= \beta_{\ell-r} u_{\ell-r} - \beta_{\ell} u_{\ell+1} + \left(\beta_{\ell} u_{\ell+1} - 2\beta_{\ell} u_{\ell} + \beta_{\ell} u_{\ell-1} \right) - \beta_{\ell} u_{\ell-1} \\
&\quad + \beta_{\ell+r} u_{\ell+r} \\
&= \beta_{\ell} u''_{\ell} a^2 + \beta_{\ell-r} u_{\ell-r} - \beta_{\ell} u_{\ell+1} + \beta_{\ell+r} u_{\ell+r} - \beta_{\ell} u_{\ell-1}.
\end{aligned}$$

Without loss of generality, we assume $r > 0$, then

$$\begin{aligned}
&\left(\beta_{\ell-r} u_{\ell-r} - 2\beta_{\ell} u_{\ell} + \beta_{\ell+r} u_{\ell+r} \right) = \beta_{\ell} u''_{\ell} a^2 + \beta_{\ell-r} u_{\ell-r} - \beta_{\ell} u_{\ell+1} + \beta_{\ell+r} u_{\ell+r} - \beta_{\ell} u_{\ell-1} \\
&= \beta_{\ell} u''_{\ell} a^2 + \left(\beta_{\ell} u_{\ell-r} - \beta_{\ell} u_{\ell-1} \right) + \left(\beta_{\ell} u_{\ell+r} - \beta_{\ell} u_{\ell+1} \right) \\
&\quad + u_{\ell+r} \sum_{t=0}^{r-1} \beta'_{\ell+t} a - u_{\ell-r} \sum_{t=0}^{r-1} \beta'_{\ell-r+t} a.
\end{aligned} \tag{2.3.18}$$

Therefore, we can handle T_2 for general k-th-neighbor-interaction range in a similar

way to that for the case of $k = 2$, and obtain that

$$|T_2| \leq \left(-\phi_{xx}(k)\right) \left(|\widetilde{c}_4| L^{-\frac{5}{2}} a^{-\frac{1}{2}} + |\widetilde{c}_5| L^{-2}\right) \|u'\|_{\ell^2}^2$$

which suggests that for $k \geq 2$

$$T_2 \geq \left(\phi_{xx}(k)\right) \left(\widetilde{c}_4 L^{-\frac{5}{2}} a^{-\frac{1}{2}} + \widetilde{c}_5 L^{-2}\right) \|u'\|_{\ell^2}^2.$$

Combining with the estimate T_1 (2.3.15), we have for any $k \geq 2$

$$\langle F_{,k}^{bqcf,lin}(u), u \rangle \geq \phi_{xx}(k) \left(k^2 + \widehat{C}_k L^{-\frac{5}{2}} a^{-\frac{1}{2}} + \widehat{C}_k L^{-2}\right) \|u'\|_{\ell^2}^2 \tag{2.3.19}$$

with $L = \widetilde{C} a^{-\frac{1}{5}}$ when $a = \frac{1}{M}$ being sufficiently small.

Thus, collecting all interactions up to the N-the Nearest Neighbor Interaction Range, we have

$$\begin{aligned} \langle F_{,}^{bqcf,lin}(u), u \rangle =& \langle F_{,1}^{bqcf,lin}(u), u \rangle + \sum_{k=2}^{N} \langle F_{,k}^{bqcf,lin}(u), u \rangle \\ \geq & \left[\phi_{xx}(1) + \sum_{k=2}^{N} \phi_{xx}(k) \left(k^2 + \widehat{C}_k L^{-\frac{5}{2}} a^{-\frac{1}{2}}\right) \right] \|u'\|_{\ell^2}^2. \end{aligned}$$

□

Meanwhile, from the proofs of Theorem 2.3.1 and Theorem 2.3.2, we can see that the bounds depend on the smoothness of β. Therefore, we aim to find the optimal types of blending function to preserve the bounds in the numerical simulations detailed in Section 4.

Remark 2.3.2. Throughout, the term 'optimal' is used to describe the conclusion that $L = \widetilde{C} a^{-\frac{1}{5}}$ is the optimal blending size for keeping coercivity of the force operator when $a = \frac{1}{M} \to 0$. The term 'optimal' in these instances describes the

smallest asymptotic order that could be expected to ensure stability. However, the analysis of consistency conditions is beyond the purview of this paper. Note that $\widehat{C}$ is dependent on the blending function, β, and the choice for potential energy, ϕ; and it is not on the lattice spacing constant, a.

Remark 2.3.3. From the inequality (2.3.19) that $\widehat{C}_k L^{-\frac{5}{2}} a^{-\frac{1}{2}}$ dominates the other terms only when the lattice spacing $a = \frac{1}{M}$ is very small. As a result, the asymptotically rate $L \sim a^{-\frac{1}{5}} = M^{\frac{1}{5}}$ might not be observed when the size of the atomistic chain is only moderately large. In this case, we suggest taking $L \sim a^{-\frac{1}{3}} = M^{\frac{1}{3}}$, which is observed in the numerical test.

2.4 Numerical Simulations

We conduct numerical experiments to verify the theoretical findings of the stability analysis.

2.4.1 Critical Strain Experiment

We consider a periodic chain with atom indices from $-M+1$ to M. For the following numerical simulations, we set $M = 2000$. The optimal blending size as found analytically in the previous section is $M^{1/5} \approx 5$. We will test to see if the numerical experiments coincide with this value.

First, we apply the uniform stretch to the atomistic chain and compute the critical strain when $F^{a,lin}$ and $F^{bqcf,lin}$ loses the coercivity. We compare the critical strain values between the atomistic model and blending models with different blending sizes and various types of blending functions. Critical strain values are the maximum value at which the atomistic chain can be stretched while the chain configuration remains stable. Mathematically, it means the maximum value while the smallest eigenvalue of $F^{\text{bqcf,lin}}$ remains positive definite. By comparing these values with the atomistic critical strain error, we obtain the optimal blending function and attempt to verify the optimal blending size of $M^{\frac{1}{5}}$ previously found.

Recall the Morse potential, $\phi(r) = D_e \times [1 - e^{-\alpha(r-r_e)}]^2$. Within its equation, we use the values $D_e = 3$ and $\alpha = 3, 4$,and 5, respectively. Recall from Figure 2.2, the local minimum value is set to $\phi(1)$ and the local height of the potential is D_e. Furthermore, as α grows larger, the more narrow the potential becomes.

We will consider our computational domain as $\Omega = (-1, 1]$ with periodic boundary conditions. The computational domain will be decomposed into atomistic, continuum, and blending subdomains following [10]. An interaction range is introduced to serve as a buffer region to simplify the treatment of periodic boundary conditions. The lattice spacing constant used had a value of $a = \frac{1}{M}$ which helped to start the blending region.

For numerical experiments, we denote the blending region, $\Omega^b = (b_1, b_2)$ for some $b_1, b_2 \in \Omega$. The numerical blending size, L, will be defined as $L = b_2 - b_1$. We can compare the numerical blending size with that found in the stability analysis.

Recall from Definition (2.2.15),

$$\beta(x) = \begin{cases} 1, & x \in \Omega^a \\ 0, & x \in \Omega^c \\ \in (0,1), & x \in \Omega^b = (b_1, b_2). \end{cases}$$

We conduct numerical experiments using a piecewise linear spline, piecewise cubic spline, and piecewise quintic spline blending function which are defined as follows:

$$\beta^{linear}(x) := \begin{cases} 1, & x \in \Omega^a, \\ 0, & x \in \Omega^c, \\ 1 - \frac{x-b_1}{L}, & x \in \Omega^b, \end{cases}$$

and

$$\beta^{cubic}(x) := \begin{cases} 1, & x \in \Omega^a, \\ 0, & x \in \Omega^c, \\ 1 + 2(\frac{x-b_1}{L})^3 - 3(\frac{x-b_1}{L})^2, & x \in \Omega^b, \end{cases}$$

and

$$\beta^{quintic}(x) := \begin{cases} 1, & x \in \Omega^a, \\ 0, & x \in \Omega^c, \\ 1 - 6(\frac{x-b_1}{L})^5 + 15(\frac{x-b_1}{L})^4 - 10(\frac{x-b_1}{L})^3 & x \in \Omega^b. \end{cases}$$

Graphical demonstrations of these various blending functions can be found in Figure 2.4.

Remark 2.4.1. It must be noted that the analysis conducted in this section only applies to the cubic or quintic blending function used in these simulations. Due to less regularities near the boundaries of the blending region, the analysis does not encompass the linear blending function. In these experiments, we can also see that the linear blending leads to the most discrepancies. We include the linear blending function, however, due to its simplicity,

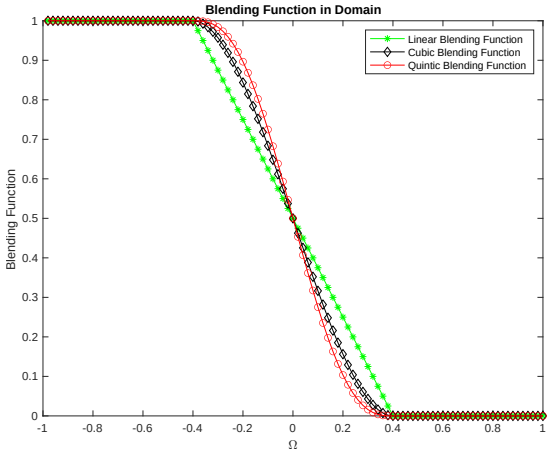

Figure 2.4: Graphical representation of the blending functions used in numerical experiments. Recall, at $\beta = 1$, the purely atomistic model is obtained and at $\beta = 0$, the purely continuum model is obtained.

We apply a uniform stretch to the atomistic chain. From this we numerically compute the critical strains of the atomistic model and compare this to the coupling model with different blending sizes to find the critical stretch value that makes the atomistic chain unstable. The step size to increase γ is $\Delta\gamma = 10^{-5}$. We also model the different values of α in the Morse Potential using the cubic blending function. As can be seen in Table 2.1, the cubic blending function reaches the atomistic critical stretch value faster than the other two blending functions; albeit just slightly quicker than the quintic blending function.

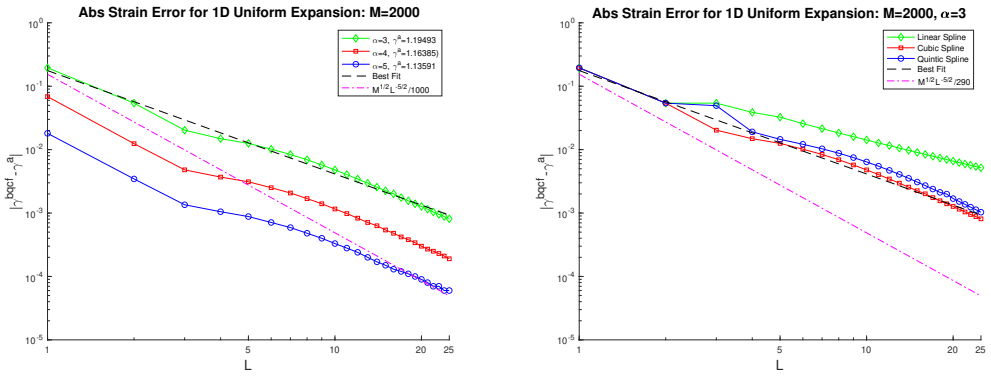

Figure 2.5: The absolute critical strain errors are plotted for the 1D uniform stretching. We set $M = 2,000$ and γ^a and γ^{bqcf} are the critical strains for the atomistic and B-QCF models, respectively. a) Models the cubic spline blending for various values of α; and b) models the critical strain errors of linear, cubic, and quintic blending functions with $M = 2,000$ and $\alpha = 3$.

The results of Table 1 suggest the blending size to be $L \approx M^{\frac{1}{3}}$. We account for this difference because of the other terms in inequality (2.3.19) when observing only a moderately large atomistic chain. For further clarification, see Remark 2.4.2.

The results from the numerical experiments find the cubic blending function as that which converges quickest toward the atomistic strain value and is thus the optimal blending function from those we tested.

Remark 2.4.2. Recall from (2.3.12), the assumption that:

$$\left(2c_3L^{-\frac{5}{2}}a^{-\frac{1}{2}} + 4c_2L^{-2} + c_1L^{-1}\right) \leq \left(c_4L^{-\frac{5}{2}}a^{-\frac{1}{2}}\right).$$

Table 2.1: Shown are the critical stretching values for linear, cubic, and quintic blending models for a blending size from a to $10a$. The critical value for the purely atomistic model was found to be $\gamma^a = 1.195$. The numerical increment for $\Delta\gamma$ is 10^{-5}.

Blend size	Linear	Cubic	Quintic
1	1	1	1
2	1.1400	1.1409	1.1409
3	1.1269	1.1747	1.1456
4	1.1562	1.1801	1.1759
5	1.1624	1.1824	1.1804
6	1.1692	1.1848	1.1828
7	1.1735	1.1866	1.1847
10	1.1811	1.1950	1.1950

The latter two terms on the left side of the inequality would not necessarily be negligible if the number of atoms M were not large enough. This accounts for the difference observed in the blending size between the analysis and the numerical simulation.

2.4.2 Simulation of Deformed Configuration

Now that we have found the cubic blending function to be the optimal blending function, we utilize this for the remaining numerical tests. We use a blending size $L = 5$, following the optimal analytical blend size found in Section 2.3, since $2000^{\frac{1}{5}} \approx 4.57$ and use $\alpha = 3$ for both numerical experiments. Next, we test two functions with periodic boundary conditions as the external force of the system to ensure that the blended coupling scheme performs as imagined.

- **First, we use a sinusoidal external force**

$$F^{ext}_{\ell,} = 0.01 \times \sin(-x_\ell \times \pi).$$

We use this function to incorporate the periodic boundary conditions.

We obtain the expected force plot for our domain as can be seen in Fig. 2.6. The displacement is also observed for an interaction range potential from

the first neighbor up to the third neighbor. We observe that the difference between an interaction range potential of $N = 2$ versus an interaction range potential of $N = 3$ is much smaller than the difference between the change in displacement for the interaction range potential for $N = 1$ and $N = 2$. Recall that the characteristics of the Morse potential are such that $\phi_{xx}(1) > 0$ and $\phi_{xx}(k) \leq 0$ for $k \geq 2$. Thus, after the next-nearest neighbor, $k = 2$, the change in displacement will not differ much.

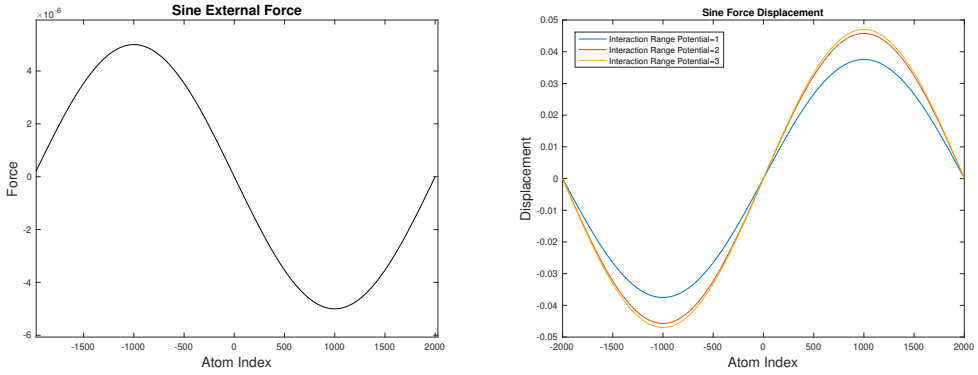

Figure 2.6: a) A sinusoidal external force is shown. b) The various displacements for this external force are displayed within the domain.

- **Next, we test a large Gaussian external force:**

$$F_{\ell,}^{ext} = 20 \times e^{\frac{-(x_\ell - \mu)^2}{2\sigma^2}},$$

where $\mu = 4$, $\sigma = 3$, and $a = 1/M$ with $M = 2000$ was used.

Again, we show the force output for our domain and show the various displacements for three interaction range potentials. Similarly to the sinusoidal external force, once the interaction range reaches a value of $N = 2$, the change in displacement becomes less significant.

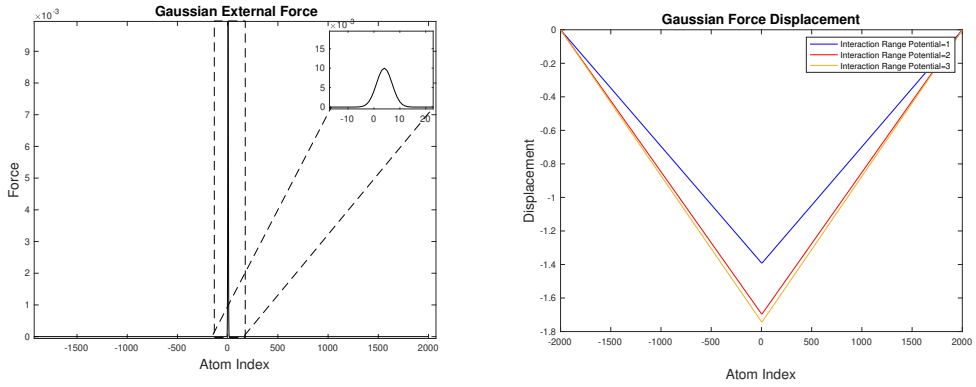

Figure 2.7: a) A Gaussian external force is shown. b) The various displacement for this external force are displayed within the domain.

2.5 Conclusion

In this chapter, inspired by the force-based coupling of the Peridynamics model of [10], we have formulated a similar symmetric and consistent blended force-based AtC coupling scheme in one-dimensional space. We were able to identify the optimal asymptotic conditions on the width of the blending region, $L \approx M^{\frac{1}{5}}$ to ensure the H^1 stability of the linearized force-based blending operator when the chain size is large enough.

We verified the theoretical findings with numerical experiments on the blending function and the blending region. From these numerical experiments, we find that the cubic blending provides the best results compared to the critical stretch of the fully atomistic model. We also find that the optimal blending width from these numerical experiments is $L \approx M^{\frac{1}{3}}$ due to non-negligible terms when not working with a large enough atomistic chain.

CHAPTER 3: Peridynamics-to-Peridynamics

3.1 Introduction

This chapter focuses on a nonlocal model, the Peridynamics model, proposed in 2000 by Dr. Stewart Silling [8]. This model uses integro-differentials and time derivatives instead of the spatial derivatives typical of classical models, which naturally allows for the simulation of defect dynamics such as crack propagation, making this a desirable model for predicting fracture. Peridynamics is also defined by the internal force interaction between material points. Additionally, PD has been used successfully to study crack branching and crack interactions (e.g., [37], [38], [39]). However, it proves to be more computationally expensive than classical mechanics models, and the treatment of boundary conditions and interfacial conditions is an ongoing challenge [40].

Classical PDE descriptions of solid mechanics provide a good approximation for many length scales; however, with an increasing demand for accuracy at smaller scales, a different formulation was necessary [41]. Peridynamics also allows for a broader solution space that allows for discontinuities due to its lack of spatial derivatives.

Dynamic simulations also bring their own set of challenges in terms of artifacts of proposed schemes. The previous chapter dealt with the nuances of a static local-to-nonlocal coupling method. The aim of this chapter is to model a bimaterial bar in dynamic situations using PD-PD to do so. Similarly to [42] and [43], we investigate the conservation of physical quantities such as momentum, energy, and reflection of the created model. When cracks propagate in a material, the underlying problem becomes dynamic, in which the prediction of the crack can be affected by

the wave propagation of the fracture energy. As the wave travels through the materials and approaches the interface, physical reflection will occur as a result of the introduction of the second material. However, when creating a scheme to model this interaction, artificial reflection can also be present as a result of the scheme itself. Thus, when modeling this system, more reflection would be shown than what is physically accurate. Therefore, we seek to reduce spurious reflection at the interface of two materials, as can be brought on by the nonlocality of the model.

Due to its nonlocality and, thus, increased computation, ongoing research focuses on coupling Peridynamics with finite element methods (FEM) [44], [45]; extended finite element methods (XFEM) [46], [47]; or classical elasticity [1], [48] to name a few. This coupling allows for a less computationally expensive model to be used away from known or suspected defects or fractures. However, such coupling requires some prior knowledge of possible fracture locations to be applied appropriately.

In Chapter 2, we created a symmetric, blended force-based method for AtC coupling. The nonlocality provided by the atomistic equation, in which the N^{th} neighbor interaction was taken into account with the displacement, is similar to Peridynamics with respect to the horizon parameter. In Peridynamic theory, there exists a nonlocal entity titled the horizon parameter and denoted by δ, in which every point in a domain interacts with every other point within its horizon through short-range force interactions [8]. This horizon term provides a length scale that allows Peridynamics to be utilized with other models to create a multiscale model [1].

It has been shown in [49] that given certain conditions in which the motion, constitutive model, and nonhomegenities are sufficiently smooth, PD converges to the classical PDE-based equation for classical elasticity is recovered. Cauchy's first

equation of motion in classical elasticity is

$$\rho(x)\ddot{u}(x,t) = \nabla\sigma(x,t) + b(x,t)$$

where σ is the stress tensor. It is thus not difficult to see how the PD equation of motion

$$\rho\ddot{u}(x,t) = \int_{H_x} f(u(y,t) - u(x,t), y - x)dV_{x'} + b(x,t), \qquad x \in \Omega$$

can recover the classical elasticity formulation. A further explanation of the PD equation of motion will follow in the next section.

Similarly, in [50] it has been shown that PD can also be seen as an upscaling of molecular dynamics (MD). Its length term and its ability to recover classical elasticity or molecular dynamics make Peridynamics extremely effective at creating multiscale models through coupling, spanning many length scales.

The combination of Peridynamics with Peridynamics proves especially important where two materials meet, as the resulting system is more susceptible to fracture near their interface. Thus, this chapter will focus on the bimaterial PD-PD scheme near the interface of the two materials.

Currently, work is being done on using Peridynamics at bimaterial interfaces. In [51], they investigate such a system using state-based Peridynamics. In this work, the various properties of the material for the cross-material interaction are explored. The various methods they test include using the material property with a smaller bulk modulus as proposed in [52], representing the material properties as Heaviside functions as proposed in [53], or using the arithmetic or harmonic average between the points utilizing their distances apart from one another as proposed in [53], [54], [55]. They found that the harmonic average worked best as a representation of this cross-material interaction. In [56], it is proposed to smoothly

transition from the elastic modulus of one material to another in the interface region. This has been found to successfully capture interface fractures. In [55], they also explored using weight functions between material properties to capture the interface interaction. The work proposed in these papers inspires our treatment of the nonlocal interface interaction kernel through numerical tests.

In this chapter, we create a Peridynamics governing equation for a bimaterial system in one dimension utilizing PD to model both materials. Then we show the conditions for momentum and energy conservation for such a system. Then, the dispersion relation is derived for each part of the domain. From this relation we estimate the coefficient of reflection near the interface of the two materials. We find numerically optimal cross-material interaction values to minimize the spurious reflection artifacts for the Peridynamics-to-Peridynamics (PD-PD) case.

The remaining chapter will be arranged as follows.

- In the remainder of this section, the notation necessary for this work will be presented. We then create the governing equations for this bimaterial system from the classical PD equation of motion.

- In Section 2, we prove that the conservation laws are preserved. We first show the necessary conditions for the conservation of momentum in Proposition 3.2.1 and then show the conditions for energy conservation in Proposition 3.2.2.

- In Section 3, we derive the reflection coefficient at $x_{I-\delta}$ in (3.3.18) and at $x_{I+\delta}$ in (3.3.19) from the simplified dispersion relations of the PD system for the different subdomains.

- In Section 4, we numerically find an optimal interaction kernel for cross-material interactions such that the PD-PD reflection and the local reflection are minimized to reduce spurious artifacts.

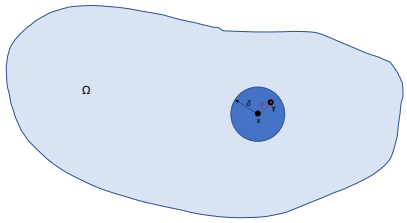

Figure 3.1: Example of a 2D domain for Peridynamics and how the horizon value works for PD.

3.1.1 Peridynamic Theory and Notation

Let $\Omega \in R^d$ be the domain for $d = 1, 2, 3$. Then, governing equation of motion for one material is

$$\rho\ddot{u}(x,t) = \int_{H_x} f(u(y,t) - u(x,t), y - x)dV_{x'} + b(x,t), \qquad x \in \Omega.$$

where ρ is the mass density, f is the pairwise force function, u is the displacement vector, δ is the horizon of the reference point x and b is the external force density. We also define the neighborhood of a point x to be

$$H_x := \{y \in R^d : \|y - x\| \leq \delta\}.$$

The work in this chapter is concerned purely with one-dimension with no body force density and thus we employ the one-dimensional linear Peridynamics equation of motion similar to [1] as follows:

$$\rho\ddot{u}(x,t) = \int_{x-\delta}^{x+\delta} \gamma(|y - x|)[u(y,t) - u(x,t)]dy, \qquad x \in \Omega. \tag{3.1.1}$$

where γ is the nonlocal interaction kernel, a parameter determined by the material.

3.1.2 Peridynamics Model for Bi-Material System

We begin by considering a one-dimensional rod with two materials that meet at an interface. The linear PD equation as presented in (3.1.1) does not capture this phenomenon, and thus we will start by defining a governing equation for this problem.

We choose a local reference domain, $\Omega_l = (0, 1)$. We split this reference domain in four parts:

- $\Omega_1 = (0, x_{I-\delta}]$-Domain described by material 1 intra-material interaction;
- Ω_*-Domain described by some intra-material interaction as well as inter-material interaction;
  - $\Omega_{*,1} = (x_{I-\delta})$-Domain described by some material 1 intra-material interaction as well as inter-material interaction;
  - $\Omega_{*,2} = (x_I, x_{I+\delta})$-Domain described by some material 2 intra-material interaction as well as inter-material interaction;
- $\Omega_2 = [x_I + \delta, 1)$-Domain described by material 2 intra-material interaction

where $\Omega_l = \Omega_1 \cup \Omega_* \cup \Omega_2$.

In 1D, the neighborhood of $x \in \Omega_l$ is defined as $H_x = (x - \delta, x + \delta)$. Due to the horizon, we define the nonlocal boundary to be $\Omega_{nl} = \Omega_{nl,1} \cup \Omega_{nl,2}$ where $\Omega_{nl,1} = (-\delta, 0)$ and $\Omega_{nl,2} = (1, 1 + \delta)$.

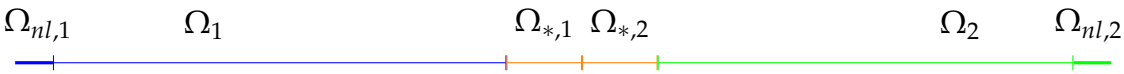

Figure 3.2: Subdomains for the 1D bimaterial formulation.

We define γ_1 as the nonlocal interaction kernel for material one, where the points in material one interact purely with other points in material one. Similarly, we define γ_2 as the nonlocal interaction kernel for material 2. For this work, as a

simplifying assumption, we utilize constant γ values. See Section 4 for a discussion on the future directions of this project for a more physically relevant representation and the associated challenges.

We then define the nonlocal interaction kernels as such:

$$\gamma_1 = \frac{K_1}{\delta^3}, \qquad \gamma_2 = \frac{K_2}{\delta^3}$$

where K_1 and K_2 are the elasticity constants for the respective materials.

We make another simplifying assumption that the materials have the same horizon value, $\delta_1 = \delta_2 = \delta$, so we will use δ throughout. See Section 4 for a discussion on ways to make this value more rigorous and physically relevant.

We also find that an interaction kernel is required for cross-material interaction within the domains $\Omega_{*,1}$ and $\Omega_{*,2}$. We denote this term by γ_*. The question of how to define γ_* is still an open problem and is explored in [51], [56], [55]. For now, we do not define this term but assume that it is a function of γ_1 and γ_2, which also makes it a constant value. Thus, we can make the simplification $\gamma(|y - x|) = \gamma$ since our use of the interaction kernel in this case is independent of where the material points are in relation to one another. In Section 4 we find numerically optimal γ_* terms for each wavenumber to reduce reflection.

Because γ_1 and γ_2 have the same horizon δ, the governing equation for this bimaterial nonlocal system is defined as

$$\rho\ddot{u}(x) := \begin{cases} \int_{x-\delta}^{x+\delta} \gamma_1[u(y) - u(x)]dy & x \in \Omega_1 \\ \int_{x-\delta}^{x_I} \gamma_1[u(y) - u(x)]dy & \\ \quad + \int_{x_I}^{x+\delta} \gamma_*[u(y) - u(x)]dy & x \in \Omega_{*,1} \\ \int_{x-\delta}^{x_I} \gamma_*[u(y) - u(x)]dy & \\ \quad + \int_{x_I}^{x+\delta} \gamma_2[u(y) - u(x)]dy & x \in \Omega_{*,2} \\ \int_{x-\delta}^{x+\delta} \gamma_2[u(y) - u(x)]dy & x \in \Omega_2. \end{cases} \tag{3.1.2}$$

This split accounts for the different bond interactions that occur among particles within one material, with particles of the same material as well as particles from different materials interacting with one another.

3.2 Conservation Laws for a Bimaterial Problem

In this section, the conservation of total momentum and total energies is ensured in this Peridynamics-to-Peridynamics bimaterial framework.

3.2.1 Conservation of Momentum

Proposition 3.2.1 (Conservation of Momentum)**.** *The momentum associated with a Peridynamics-to-Peridynamics bimaterial framework is conserved when*

$$\int_0^{\delta}\int_{x-\delta}^{0}\gamma_1[u(y)-u(x)]dydx+\int_{1-\delta}^{1}\int_{1}^{x+\delta}\gamma_2[u(y)-u(x)]dydx=0. \tag{3.2.1}$$

Proof. We intend to check when the momentum is conserved. We integrate the governing equation, (3.1.2), over the local domain, $\Omega_l=(0,1)$, in x.

$$\int_0^1\rho\ddot{u}(x)dx=\begin{cases}\int_0^{x_I-\delta}\int_{x-\delta}^{x+\delta}\gamma_1[u(y)-u(x)]dydx & x\in\Omega_1\\ \int_{x_I-\delta}^{x_I}\int_{x-\delta}^{x_I}\gamma_1[u(y)-u(x)]dydx & \\ \quad+\int_{x_I-\delta}^{x_I}\int_{x_I}^{x+\delta}\gamma_*[u(y)-u(x)]dydx & x\in\Omega_{*,1}\\ \int_{x_I}^{x_I+\delta}\int_{x-\delta}^{x_I}\gamma_*[u(y)-u(x)]dydx & \\ \quad+\int_{x_I}^{x_I+\delta}\int_{x_I}^{x+\delta}\gamma_2[u(y)-u(x)]dydx & x\in\Omega_{*,2}\\ \int_{x_I+\delta}^{1}\int_{x-\delta}^{x+\delta}\gamma_2[u(y)-u(x)]dydx & x\in\Omega_2\end{cases} \tag{3.2.2}$$

We first extend our attention to the left-hand side of the equation

$$\int_0^1\rho\ddot{u}dx=\frac{\partial}{\partial t}\int_0^1\rho\frac{\partial u}{\partial t}dx. \tag{3.2.3}$$

Note that $\rho\frac{\partial u}{\partial t}$ represents the momentum of the system and, thus, we wish to

observe when

$$\frac{\partial}{\partial t}\int_0^1 \rho \frac{\partial u}{\partial t} dx = 0.$$

Isolating the equations for $x \in \Omega_1 \cup \Omega_{*,1}$ such that only γ_1 is used, we tend to the following

$$\int_0^{x_I-\delta}\int_{x-\delta}^{x+\delta} \gamma_1[u(y)-u(x)]dydx + \int_{x_I-\delta}^{x_I}\int_{x-\delta}^{x_I} \gamma_1[u(y)-u(x)]dydx. \tag{3.2.4}$$

We see that $\gamma_1[u(y)-u(x)]$ is an odd function, so when $(x \in \Omega_1 \cup \Omega_{*,1}) \cap (y \in \Omega_{nl} \cup \Omega_1 \cup \Omega_{*,1})$, the integral is 0. However, when x is in $(0,\delta)$, it also interacts with points, y, in the nonlocal domain, $\Omega_{nl,1} = (-\delta, 0)$. Hence, the resulting integral for $x \in \Omega_1$ is:

$$\begin{aligned}\int_0^{x_I-\delta}\int_{x-\delta}^{x+\delta} \gamma_1[u(y)-u(x)]dydx + \int_{x_I-\delta}^{x_I}\int_{x-\delta}^{x_I} \gamma_1[u(y)-u(x)]dydx \\ = \int_0^{\delta}\int_{x-\delta}^{0} \gamma_1[u(y)-u(x)]dydx.\end{aligned} \tag{3.2.5}$$

The case for $x \in \Omega_2 \cup \Omega_{*,2}$ such that only γ_2 is used, is treated similarly to (3.2.4),

$$\begin{aligned}\int_{x_I}^{x_I+\delta}\int_{x_I}^{x+\delta} \gamma_2[u(y)-u(x)]dydx + \int_{x_I+\delta}^{1}\int_{x-\delta}^{x+\delta} \gamma_2[u(y)-u(x)]dydx \\ = \int_{1-\delta}^{1}\int_{1}^{x+\delta} \gamma_2[u(y)-u(x)]dydx.\end{aligned} \tag{3.2.6}$$

Finally, we focus on $x \in \Omega_{*,1} \cup \Omega_{*,2}$ so that only γ_* is used. Recall that γ_* details the intermaterial interaction.

$$\int_{x_I-\delta}^{x_I}\int_{x_I}^{x+\delta} \gamma_*[u(y)-u(x)]dydx + \int_{x_I}^{x_I+\delta}\int_{x-\delta}^{x_I} \gamma_*[u(y)-u(x)]dydx \tag{3.2.7}$$

Focusing on the first integral of (3.2.7), we exchange variables and thus adjust

the bounds of integration accordingly

$$\begin{aligned}\int_{x_I-\delta}^{x_I}\int_{x_I}^{x+\delta}\gamma_*[u(y)-u(x)]dydx &= \int_{x_I-\delta}^{x_I}\int_{x_I}^{y+\delta}\gamma_*[u(x)-u(y)]dxdy \\ &= -\int_{x_I}^{x_I+\delta}\int_{x-\delta}^{x_I}\gamma_*[u(y)-u(x)]dydx.\end{aligned} \tag{3.2.8}$$

Thus (3.2.7) becomes,

$$\int_{x_I-\delta}^{x_I}\int_{x_I}^{x+\delta}\gamma_*[u(y)-u(x)]dydx + \int_{x_I}^{x_I+\delta}\int_{x-\delta}^{x_I}\gamma_*[u(y)-u(x)]dydx = 0.$$

Hence, when momentum is conserved and $\frac{\partial}{\partial t}\int_0^1 \rho\frac{\partial u}{\partial t}dx = 0$, the resultant becomes

$$\int_0^{\delta}\int_{x-\delta}^{0}\gamma_1[u(y)-u(x)]dydx + \int_{1-\delta}^{1}\int_1^{x+\delta}\gamma_2[u(y)-u(x)]dydx = 0 \tag{3.2.9}$$

□

3.2.2 Conservation of Energy

Proposition 3.2.2 (Conservation of Energy)**.** *The total energies associated with a Peridynamics-to-Peridynamics bimaterial framework is conserved when*

$$\begin{aligned}\int_0^{\delta}\int_{x-d}^{0}\gamma_1[u(y)-u(x)]\dot{u}(x)dydx \\ + \int_{1-\delta}^{1}\int_1^{x+\delta}\gamma_1[u(y)-u(x)]\dot{u}(x)dydx = 0.\end{aligned} \tag{3.2.10}$$

Proof. We intend to check when the conservation of energy is observed in this scenario. The expected total energies for this bimaterial system in this nonlocal case

is defined as follows:

$$
\begin{aligned}
TotalEnergy := \\
&\Big[\int_0^1 \frac{\rho}{2}(\frac{\partial u}{\partial t})^2 dx\Big] + \frac{1}{4}\int_0^{x_I}\int_0^{x_I} \gamma_1[u(y)-u(x)]^2 dydx \\
&+ \frac{1}{4}\int_{x_I}^1\int_{x_I}^1 \gamma_2[u(y)-u(x)]^2 dydx \\
&+ \frac{1}{4}\int_{x_I-\delta}^{x_I}\int_{x_I}^{x+\delta} \gamma_*[u(y)-u(x)]^2 dydx \\
&+ \frac{1}{4}\int_{x_I}^{x_I+\delta}\int_{x-\delta}^{x_I} \gamma_*[u(y)-u(x)]^2 dydx
\end{aligned}
\tag{3.2.11}
$$

where $\Big[\int_0^1 \frac{\rho}{2}(\frac{\partial u}{\partial t})^2\Big]$ is the kinetic energy contribution and the subsequent terms represent the nonlocal elastic energy contributions to the total energies.

From the equation of motion (3.1.2), we integrate over the local domain, $\Omega_l = (0,1)$, in x and multiply by velocity at the reference value x. In order to investigate the conservation of energy, we sum the contributing terms:

$$
\begin{aligned}
\int_0^1 \rho\ddot{u}(x)\dot{u}(x)dx = &\int_0^{x_I-\delta}\int_{x-\delta}^{x+\delta} \gamma_1[u(y)-u(x)]\dot{u}(x)dydx \\
&+ \int_{x_I-\delta}^{x_I}\int_{x-\delta}^{x_I} \gamma_1[u(y)-u(x)]\dot{u}(x)dydx \\
&+ \int_{x_I-\delta}^{x_I}\int_{x_I}^{x+\delta} \gamma_*[u(y)-u(x)]\dot{u}(x)dydx \\
&+ \int_{x_I}^{x_I+\delta}\int_{x-\delta}^{x_I} \gamma_*[u(y)-u(x)]\dot{u}(x)dydx \\
&+ \int_{x_I}^{x_I+\delta}\int_{x_I}^{x+\delta} \gamma_2[u(y)-u(x)]\dot{u}(x)dydx \\
&+ \int_{x_I+\delta}^{1}\int_{x-\delta}^{x+\delta} \gamma_2[u(y)-u(x)]\dot{u}(x)dydx.
\end{aligned}
\tag{3.2.12}
$$

We first extend our attention to the left-hand side of the equation using the chain rule for derivatives

$$
\int_0^1 \rho\ddot{u}(x)\dot{u}(x)dx = \frac{\partial}{\partial t}\left[\int_0^1 \frac{\rho}{2}(\frac{\partial u}{\partial t})^2 dx\right] \tag{3.2.13}
$$

and thus obtaining the time derivative of the kinetic energy.

Isolating the equations for $x \in \Omega_1 \cup \Omega_{*,1}$ such that only γ_1 is used, we tend to the following

$$\int_0^{x_I-\delta} \int_{x-\delta}^{x+\delta} \gamma_1[u(y)-u(x)]\dot{u}(x)dydx + \int_{x_I-\delta}^{x_I} \int_{x-\delta}^{x_I} \gamma_1[u(y)-u(x)]\dot{u}(x)dydx.$$

Similarly to Section 2, we first focus where the bounds of integration for x, y overlap and switch the variables and adjust the bounds of integration accordingly

$$\begin{aligned}
&\int_0^{x_I} \int_0^{x_I} \gamma_1[u(y)-u(x)]\dot{u}(x)dydx \\
&\qquad = \frac{1}{2}\int_0^{x_I} \int_0^{x_I} \gamma_1[u(y)-u(x)]\dot{u}(x)dydx \\
&\qquad\quad + \frac{1}{2}\int_0^{x_I} \int_0^{x_I} \gamma_1[u(y)-u(x)]\dot{u}(x)dydx \\
&\qquad = \frac{1}{2}\int_0^{x_I} \int_0^{x_I} \gamma_1[u(y)-u(x)]\dot{u}(x)dydx \\
&\qquad\quad + \frac{1}{2}\int_0^{x_I} \int_0^{x_I} \gamma_1[u(x)-u(y)]\dot{u}(y)dxdy \\
&\qquad = \frac{1}{2}\int_0^{x_I} \int_0^{x_I} \gamma_1[u(y)-u(x)]\dot{u}(x)dydx \\
&\qquad\quad - \frac{1}{2}\int_0^{x_I} \int_0^{x_I} \gamma_1[u(y)-u(x)]\dot{u}(y)dydx \\
&\qquad = -\frac{1}{2}\int_0^{x_I} \int_0^{x_I} \gamma_1[u(y)-u(x)][\dot{u}(y)-\dot{u}(x)]dydx \\
&\qquad = -\frac{1}{4}\frac{\partial}{\partial t}\int_0^{x_I} \int_0^{x_I} \gamma_1[u(y)-u(x)]^2 dydx.
\end{aligned} \tag{3.2.14}$$

We notice that this is one of the nonlocal elastic energy contributions that contains the γ_1 term.

Where the bounds of integration do not overlap in this region, we are left with a nonlocal boundary term

$$\int_0^{\delta} \int_{x-\delta}^{0} \gamma_1[u(y)-u(x)]\dot{u}(x)dydx. \tag{3.2.15}$$

We next treat the equations where $x \in \Omega_2 \cup \Omega_{*,2}$ that use only nonlocal interaction kernel γ_2 similarly to (3.2.14) when the bounds of integration for x, y overlap,

$$\begin{aligned}
&\int_{x_I}^{x_I+\delta} \int_{x_I}^{x+\delta} \gamma_2[u(y)-u(x)]\dot{u}(x)dydx \\
&\quad + \int_{x_I+\delta}^{1} \int_{x-\delta}^{x+\delta} \gamma_2[u(y)-u(x)]\dot{u}(x)dydx \\
&= -\frac{1}{4}\frac{\partial}{\partial t}\int_{x_I}^{1}\int_{x_I}^{1} \gamma_2[u(y)-u(x)]^2 dydx \\
&\quad + \int_{1-\delta}^{1}\int_{1}^{x+\delta} \gamma_1[u(y)-u(x)]\dot{u}(x)dydx.
\end{aligned} \tag{3.2.16}$$

Again, where the bounds of integration do not overlap, we are left with the other nonlocal boundary term

$$\int_{1-\delta}^{1}\int_{1}^{x+\delta} \gamma_1[u(y)-u(x)]\dot{u}(x)dydx. \tag{3.2.17}$$

We now draw our attention to the remaining part of (3.2.12) on the terms where $x \in \Omega_{*,1}$ such that γ_* is utilized

$$\begin{aligned}
&\int_{x_I-\delta}^{x_I} \int_{x_I}^{x+\delta} \gamma_*[u(y)-u(x)]\dot{u}(x)dydx \\
&+ \int_{x_I}^{x_I+\delta} \int_{x-\delta}^{x_I} \gamma_*[u(y)-u(x)]\dot{u}(x)dydx.
\end{aligned} \tag{3.2.18}$$

Focusing on the first part of (3.2.18), following the work of (3.2.8), we switch the

variables and change the order of integration of the first double integral

$$\begin{aligned}
&\int_{x_I-\delta}^{x_I}\int_{x_I}^{x+\delta}\gamma_*[u(y)-u(x)]\dot{u}(x)dydx\\
&=\frac{1}{2}\int_{x_I-\delta}^{x_I}\int_{x_I}^{x+\delta}\gamma_*[u(y)-u(x)]\dot{u}(x)dydx\\
&\quad+\frac{1}{2}\int_{x_I-\delta}^{x_I}\int_{x_I}^{x+\delta}\gamma_*[u(y)-u(x)]\dot{u}(x)dydx\\
&=\frac{1}{2}\int_{x_I-\delta}^{x_I}\int_{x_I}^{y+\delta}\gamma_*[u(x)-u(y)]\dot{u}(x)dxdy\\
&\quad+\frac{1}{2}\int_{x_I-\delta}^{x_I}\int_{x_I}^{x+\delta}\gamma_*[u(y)-u(x)]\dot{u}(x)dydx\\
&=-\frac{1}{4}\frac{\partial}{\partial t}\int_{x_I-\delta}^{x_I}\int_{x_I}^{x+\delta}\gamma_*[u(y)-u(x)]^2dydx.
\end{aligned}\tag{3.2.19}$$

Treating the second part of (3.2.18) similarly, we obtain

$$\begin{aligned}
&\int_{x_I}^{x_I+\delta}\int_{x-\delta}^{x_I}\gamma_*[u(y)-u(x)]\dot{u}(x)dydx\\
&\qquad=-\frac{1}{4}\frac{\partial}{\partial t}\int_{x_I}^{x_I+\delta}\int_{x-\delta}^{x_I}\gamma_*[u(y)-u(x)]^2dydx.
\end{aligned}\tag{3.2.20}$$

Thus, we obtain the following where the time derivative of the total energy for

this nonlocal case are summed,

$$\begin{aligned}
&\frac{\partial}{\partial t}\Bigg[\int_0^1 \frac{\rho}{2}(\frac{\partial u}{\partial t})^2 dx \\
&\quad + \frac{1}{4}\int_0^{x_I}\int_0^{x_I} \gamma_1[u(y)-u(x)]^2 dydx \\
&\quad + \frac{1}{4}\int_{x_I}^1\int_{x_I}^1 \gamma_2[u(y)-u(x)]^2 dydx \\
&\quad + \frac{1}{4}\int_{x_I-\delta}^{x_I}\int_{x_I}^{x+\delta} \gamma_*[u(y)-u(x)]^2 dydx \\
&\quad + \frac{1}{4}\int_{x_I}^{x_I+\delta}\int_{x-\delta}^{x_I} \gamma_*[u(y)-u(x)]^2 dydx\Bigg] \\
&= \int_0^{\delta}\int_{x-d}^0 \gamma_1[u(y)-u(x)]\dot{u}(x) dydx \\
&\quad + \int_{1-\delta}^1\int_1^{x+\delta} \gamma_1[u(y)-u(x)]\dot{u}(x) dydx
\end{aligned} \tag{3.2.21}$$

Therefore, when energy is conserved the resultant becomes

$$\begin{aligned}
&\int_0^{\delta}\int_{x-d}^0 \gamma_1[u(y)-u(x)]\dot{u}(x) dydx \\
&\quad + \int_{1-\delta}^1\int_1^{x+\delta} \gamma_1[u(y)-u(x)]\dot{u}(x) dydx = 0
\end{aligned} \tag{3.2.22}$$

□

Thus, we have shown the conditions when momentum and energy are conserved.

Remark 3.2.1. The key step for conservation laws is to preserve these symmetries at the modeling level, which motivates the formulation of governing equation (3.1.2) over the interfacial region $\Omega_{*,1}$ and $\Omega_{*,2}$.

3.3 Reflection Coefficient

Inspired by the work in [42], where wave propagation was studied with a PD-FEM coupling, we similarly compute the coefficient of reflection from the dispersion relation. One of the main challenges of studying dynamics is spurious arti-

facts. In our case, we focus on the spurious reflection created using the PD-PD scheme and attempt to minimize this for a more accurate use.

3.3.1 Dispersion Relation

For the remainder of this chapter, we simplify the domain regions in the following way.

- $x \in \Omega_1 = (0, x_I - \delta)$, only γ_1 is utilized for intra-material interaction;
- $x \in \Omega_* = (x_I - \delta, x_I + \delta)$, only γ_* is utilized for inter-material interaction; and
- $x \in \Omega_2 = (x_{I+\delta,1})$, only γ_2 is utilized for intra-material interaction.

The main departure from the previous notation is that we simplify the domain, Ω_*, to include only the cross-material interaction.

We focus our attention on $x \in \Omega_1$. The work for the remaining domains is not shown since they follow similarly. In this region, the linear PD equation of motion is

$$\rho \ddot{u} = \int_{x-\delta}^{x+\delta} \gamma_1 [u(y,t) - u(x,t)] dy. \tag{3.3.1}$$

The following wave equation is used for u in this region

$$u(x,t) = e^{i(\omega t - k_1 x)}$$

where ω is the angular frequency and k_1 is the wave number for a wave in this region.

Then we can compute the left-hand side of the equation

$$\begin{aligned} \rho \ddot{u} &= \rho \left(\frac{\partial^2}{\partial t^2} (e^{i(\omega t - k_1 x)}) \right) \\ &= -\rho \omega^2 e^{i(\omega t - k_1 x)}. \end{aligned} \tag{3.3.2}$$

Next, we focus on the right-hand side of (3.3.1) by integrating. Recall that we assume constant γ values.

$$\begin{aligned}\int_{x-\delta}^{x+\delta} \gamma_1[u(y,t)-u(x,t)]dy &= \gamma_1 \int_{x-\delta}^{x+\delta} [e^{i(\omega t-k_1 y)} - e^{i(\omega t-k_1 x)}]dy \\ &= \gamma_1 \left[e^{i(\omega t-k_1 y)} \left(\frac{1}{-ik_1}\right) - y e^{i(\omega t-k_1 x)} \right]_{x-\delta}^{x+\delta} \\ &= \gamma_1 \left[e^{i(\omega t-k_1 x)}(e^{-ik_1\delta} - e^{ik_1 d}) \left(\frac{-1}{ik_1}\right) - 2\delta e^{i(\omega t-k_1 x)} \right].\end{aligned} \tag{3.3.3}$$

Reconstituting (3.3.1) from (3.3.2) and (3.3.3), we have

$$\begin{aligned}-\rho\omega^2 e^{i(\omega t-k_1 x)} &= \gamma_1 \left[e^{i(\omega t-k_1 x)}(e^{-ik_1\delta} - e^{ik_1 d}) \left(\frac{-1}{ik_1}\right) - 2\delta e^{i(\omega t-k_1 x)} \right] \\ -\rho\omega^2 &= \gamma_1 \left[\frac{-1}{ik_1}(e^{-ik_1 d} - e^{ik_1 d}) - 2\delta \right].\end{aligned} \tag{3.3.4}$$

Finally, using an inverse Euler's formula, $2isin(t) = e^{it} - e^{-it}$, we obtain the relation

$$\begin{aligned}-\rho\omega^2 &= \gamma_1 \left[\frac{-1}{ik_1}(e^{-ik_1 d} - e^{ik_1 d}) - 2\delta \right] \\ -\rho\omega^2 &= \gamma_1 \left[-2isin(k_1 d)(\frac{-1}{ik_1}) - 2\delta \right] \\ -\rho\omega^2 &= 2\gamma_1 \left[\frac{sin(k_1\delta)}{k_1} - \delta \right]\end{aligned} \tag{3.3.5}$$

Thus, the dispersion relation for each region is given by

$$-\rho\omega^2 = \begin{cases} 2\gamma_1 \left(\frac{\sin(k_1\delta)}{k_1} - \delta\right), \ x \in \Omega_1; \\ 2\gamma_* \left(\frac{\sin(k_2\delta)}{k_2} - \delta\right), \ x \in \Omega_*; \\ 2\gamma_2 \left(\frac{\sin(k_3\delta)}{k_3} - \delta\right), \ x \in \Omega_2. \end{cases} \tag{3.3.6}$$

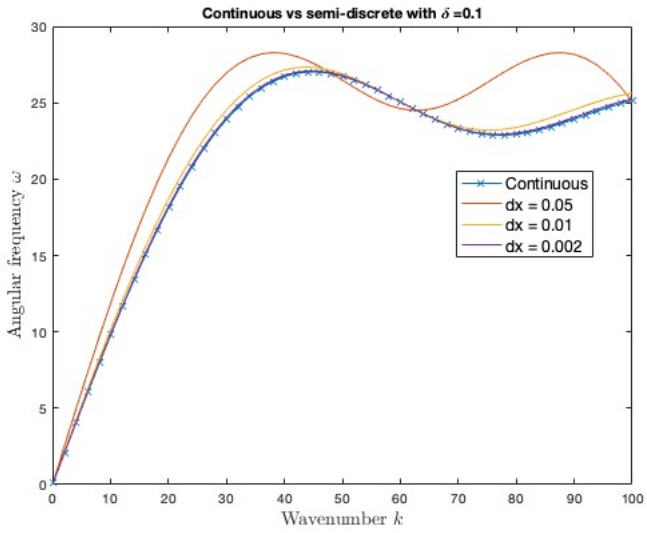

Figure 3.3: The continuous dispersion relation is compared to the semi-discrete dispersion relation with $\delta = .1$.

Due to the continuity of angular frequency ω, we have that at $x_{I-\delta}$

$$2\gamma_1 \left(\frac{\sin(k_1\delta)}{k_1} - \delta \right) = 2\gamma_* \left(\frac{\sin(k_2\delta)}{k_2} - \delta \right). \tag{3.3.7}$$

Similarly, at $x_{I+\delta}$, we have

$$2\gamma_* \left(\frac{\sin(k_2\delta)}{k_2} - \delta \right) = 2\gamma_2 \left(\frac{\sin(k_3\delta)}{k_3} - \delta \right). \tag{3.3.8}$$

In Fig. 3.3, we plot the continuous dispersion relation with the semi-discrete dispersion relation with $\delta = .1$. The various semi-discrete dispersion relations utilize different spacing values, dx. The ratio between the horizon and the grid size is indicative of computational expense and accuracy [57]. Note that for these values, the ratio is $\frac{.1}{.05} = 2$, $\frac{.1}{.01} = 10$, and $\frac{.1}{.002} = 50$. We see that as the ratios grow larger, the closer the semi-discrete dispersion relation becomes to the continuous one; however, the computational demand also grows larger. Thus, as we look to create a numerical scheme that preserves the conservation laws and reduces nu-

merical artifacts, this ratio must be taken into account for the accuracy/efficiency trade-off.

3.3.2 Derivation of Reflection Coefficients

We now focus our attention on the derivation of a reflection coefficient at $x_I - \delta$. Due to the nonlocality of PD with the horizon term δ, we notice that the intra-material interaction becomes a factor starting at this point. We omit the work for finding the coefficient of reflection at $x_I + \delta$ since it closely follows the upcoming work.

We consider a plane wave passing the first interface $x_* := x_I - \delta$. Following the formulation presented in [42], we create the wave expression without loss of generality as

$$u(x,t) = \begin{cases} e^{i(\omega t - k_1 x)} - \beta e^{i(\omega t + k_1 x)}, \ x < x_I - \delta, \\ \alpha e^{i(\omega t - k_2 x)}, \ x > x_I - \delta. \end{cases} \tag{3.3.9}$$

where the incident amplitude is 1, β is the reflection coefficient and α is the transmitted coefficient. Ultimately, we seek to estimate β for our PD-PD system at $x_{I-\delta}$.

Due to the continuity of the wave at $x_I - \delta$, we have the following relation

$$1 - \beta = \alpha.$$

Also, to simplify the calculation and without loss of generality, we assume that $x_I = \delta$ and $\rho = 1$ and consider the force equation at $x_* = x_I - \delta = 0$.

Focusing on the left side of the PD force equation for a wave as it approaches $x_I - \delta$,

$$\ddot{u}(x_*, t) = (-\omega^2) e^{i(\omega t)}. \tag{3.3.10}$$

Now, focusing on the right side of the PD force equation at $x_I - \delta = 0$,

$$\begin{aligned}\int_{x-\delta}^{x_I-\delta} \gamma_1 u(y) - u(x)]dy + \int_{x_I-\delta}^{x+\delta} \gamma_*[u(y) - u(x)]dy \\ = \int_{-\delta}^{0} \gamma_1[u(y) - u(x)]dy + \int_{0}^{\delta} \gamma_*[u(y) - u(x)]dy\end{aligned} \tag{3.3.11}$$

Then making a substitution in the first equation for $s = x - y$ and in the second equation for $s = x + y$, we obtain the following integral

$$\begin{aligned}\int_{-\delta}^{0} \gamma_1[u(y) - u(x)]dy + \int_{0}^{\delta} \gamma_*[u(y) - u(x)]dy \\ = \int_0^\delta \gamma_1\Big(u(x-s) - u(x)\Big)ds + \int_0^\delta \gamma_*\Big(u(x+s) - u(x)\Big)ds\end{aligned} \tag{3.3.12}$$

Inserting the plane wave from (3.3.9), the integral becomes

$$\begin{aligned}\int_0^\delta \gamma_1\Big(u(x-s) - u(x)\Big)ds + \int_0^\delta \gamma_*\Big(u(x+s) - u(x)\Big)ds \\ = \int_0^\delta \gamma_1\Big(e^{i(\omega t + k_1 s)} - \beta e^{i(\omega t - k_1 s)} - (1-\beta)e^{i(\omega t)}\Big)ds \\ + \int_0^\delta \gamma_*\Big(\alpha e^{i(\omega t - k_2 s)} - \alpha e^{i(\omega t)}\Big)ds.\end{aligned} \tag{3.3.13}$$

Hence, setting (3.3.10) equal to (3.3.13) as in the linearized PD equation of motion and then integrating we obtain,

$$\begin{aligned}-\omega^2 = \int_0^\delta \gamma_1\Big(e^{i(k_1 s)} - \beta e^{i(-k_1 s)} - (1-\beta)\Big)ds + \int_0^\delta \gamma_*\Big(\alpha e^{i(-k_2 s)} - \alpha\Big)ds \\ = \gamma_1\left(\frac{1}{ik_1}(e^{ik_1\delta} - 1) + \frac{\beta}{ik_1}(e^{-ik_1\delta} - 1) - (1-\beta)\delta\right) + \gamma_*\alpha\left(\frac{1}{-ik_2}(e^{-ik_2\delta}) - \delta\right).\end{aligned} \tag{3.3.14}$$

Then, we utilize Euler's formula $e^{it} = cos(t) + isin(t)$ and simplify

$$\begin{aligned}
-\omega^2 =& \frac{\gamma_1}{ik_1}(cos(k_1\delta) + isin(k_1\delta) - 1) + \frac{\beta\gamma_1}{ik_1}(cos(k_1\delta) - isin(k_1\delta) - 1) \\
&- (1-\beta)\gamma_1\delta - \frac{\gamma_*(1-\beta)}{ik_2}(cos(k_2\delta) - isin(k_2\delta) - 1) - \gamma_*(1-\beta)\delta \\
=& \frac{\gamma_1}{ik_1}(cos(k_1\delta) - 1) + \frac{\beta\gamma_1}{ik_1}(cos(k_1\delta) - 1) - \frac{\gamma_*(1-\beta)}{ik_2}(cos(k_2\delta) - 1) \\
&+ \gamma_1(1-\beta)(\frac{sin(k_1\delta)}{k_1\delta} - \delta) + \gamma_*(1-\beta)(\frac{sin(k_2\delta)}{k_2\delta} - \delta)
\end{aligned} \tag{3.3.15}$$

Using the dispersion relation at $x_I - \delta$

$$\begin{aligned}
-\omega^2 &= 2\gamma_1\left(\frac{\sin(k_1\delta)}{k_1} - \delta\right) = 2\gamma_*\left(\frac{\sin(k_2\delta)}{k_2} - \delta\right) \\
&= \gamma_1\left(\frac{\sin(k_1\delta)}{k_1} - \delta\right) + \gamma_*\left(\frac{\sin(k_2\delta)}{k_2} - \delta\right)
\end{aligned} \tag{3.3.16}$$

Hence, given k_1, we can set up the following equation for β:

$$\begin{aligned}
&\gamma_1\left(\frac{\sin(k_1\delta)}{k_1} - \delta\right) + \gamma_*\left(\frac{\sin(k_2\delta)}{k_2} - \delta\right) \\
&= \frac{\gamma_1}{ik_1}(cos(k_1\delta) - 1) + \frac{\beta\gamma_1}{ik_1}(cos(k_1\delta) - 1) - \frac{\gamma_*(1-\beta)}{ik_2}(cos(k_2\delta) - 1) \\
&\quad + \gamma_1(1-\beta)(\frac{sin(k_1\delta)}{k_1\delta} - \delta) + \gamma_*(1-\beta)(\frac{sin(k_2\delta)}{k_2\delta} - \delta).
\end{aligned} \tag{3.3.17}$$

Finally, we can solve for β at $x = x_I - \delta$, which is

$$\beta = \frac{\frac{\gamma_*}{ik_2}\Big(\cos(k_2\delta) - 1\Big) - \frac{\gamma_1}{ik_1}\Big(\cos(k_1\delta) - 1\Big)}{-\gamma_*\left(\frac{\sin(k_2\delta)}{k_2} - \delta\right) - \gamma_1\left(\frac{\sin(k_1\delta)}{k_1} - \delta\right) + \frac{\gamma_1}{ik_1}\Big(\cos(k_1\delta) - 1\Big) + \frac{\gamma_*}{ik_2}\Big(\cos(k_2\delta) - 1\Big)}. \tag{3.3.18}$$

Similarly, we can solve for $\tilde{\beta}$ at $x = x_I + \delta$, we have

$$\tilde{\beta} = \frac{\frac{\gamma_2}{ik_3}\Big(\cos(k_3\delta) - 1\Big) - \frac{\gamma_*}{ik_2}\Big(\cos(k_2\delta) - 1\Big)}{-\gamma_2\left(\frac{\sin(k_3\delta)}{k_3} - \delta\right) - \gamma_*\left(\frac{\sin(k_2\delta)}{k_2} - \delta\right) + \frac{\gamma_*}{ik_2}\Big(\cos(k_2\delta) - 1\Big) + \frac{\gamma_2}{ik_3}\Big(\cos(k_3\delta) - 1\Big)}, \tag{3.3.19}$$

where k_2 and k_3 satisfy (3.3.7).

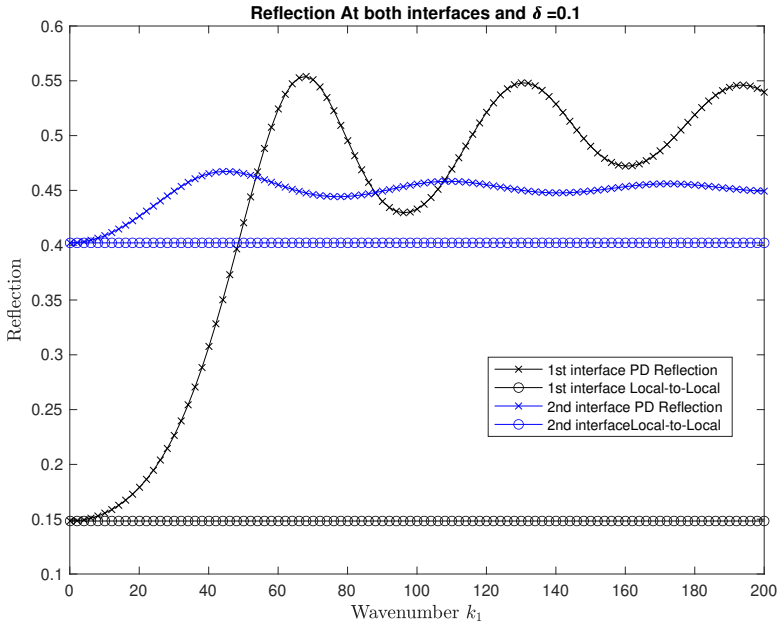

Figure 3.4: Comparison of the PD-PD Reflection at the 1st interface at $x_{I-\delta}$ (Black plots) with the local reflection at that interface and the PD-PD Reflection at the second interface $x_{I+\delta}$ (Blue plots) with the local reflection at that interface

We can see the comparison between the local reflection and the PD-PD reflection as estimated in Fig. 3.4. In this simulation, we use the harmonic average of the interaction kernel of each material to obtain γ_*, that is, $\gamma_* = \frac{2}{\frac{1}{\gamma_1}+\frac{1}{\gamma_2}}$. For both interface locations, $x_I - \delta$ and $x_I + \delta$, the local and PD-PD reflections are similar and then diverge as the wave number increases.

3.4 Optimal Cross-Material Interaction Kernel

In this section, we investigate the optimal cross-material interaction kernel to reduce reflection artifacts due to the nonlocality of this PD-PD scheme. So far,

we have assumed that γ_* is a function of γ_1 and γ_2. In [51], it is suggested that the cross-material interaction term could be defined as the common mean or the harmonic mean of the interaction term for each material. We explore this idea as well as an minimization of reflection to compare.

First, we define the overall reflection of this system as the magnitude of the maximum reflection between the two interface values of interest, $x_I + \delta$ and $x_I - \delta$. W Thus, using a step size of .01, we find the optimal γ_* value between γ_1 and γ_2 to reduce reflection. For this simulation we use $K_1 = 1$, $K_2 = 2$, and $\delta = .1$ such that

$$\gamma_1 = \frac{K1}{\delta^3} = \frac{1}{.1^3} = 1000$$

and

$$\gamma_2 = \frac{K2}{\delta^3} = \frac{4}{.1^3} = 4000.$$

We also use wavenumbers, k_1 from 0 to 100 and use the dispersion relation (3.3.6) to find the associated wavenumbers, k_2 and k_3.

We find the reflection at both interface values for every value of γ_* using (3.3.18) and (3.3.19). From this, the overall reflection is found. Finally, for each wavenumber k_1 we find the γ_* value that minimizes reflection. The result of this work can be found in Fig. 3.5. We can use this figure to compare these optimal values with the two suggested mean values for $gamma_*$. We can see that the harmonic mean performs better than the common mean.

3.5 Conclusion

In this chapter, we create the equation of motion for a bimaterial system in one dimension, introducing a cross-material interaction term. We were able to show the conditions under which energy and momentum were conserved. We were also able to find an optimal cross-material interaction term for each wave number as a function of the interaction terms for each material. We have shown numerically

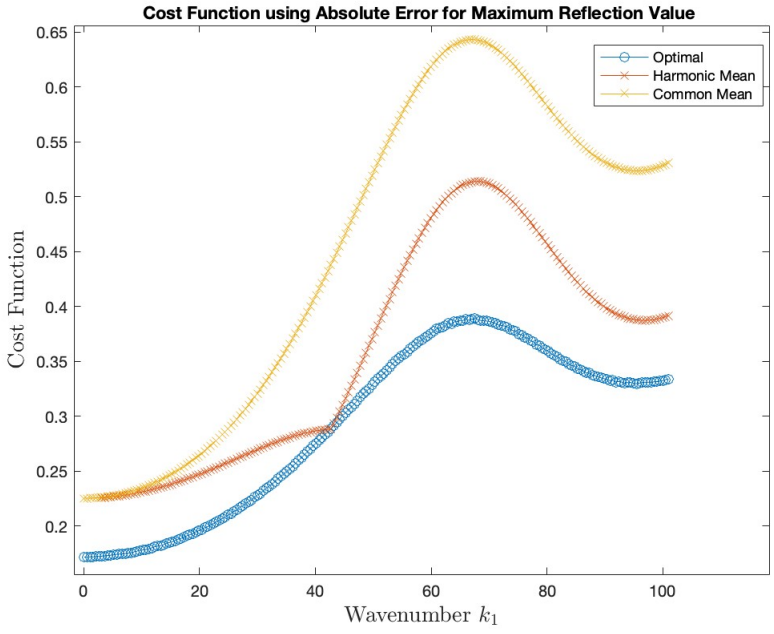

Figure 3.5: The cost function value of the optimal interaction kernel, γ_*, value found for each wave number k_1 that minimizes the nonlocal reflection against using the harmonic mean or common mean from the two material kernel values. The overall reflection was obtained by taking the maximum of the reflection coefficients at both interface values.

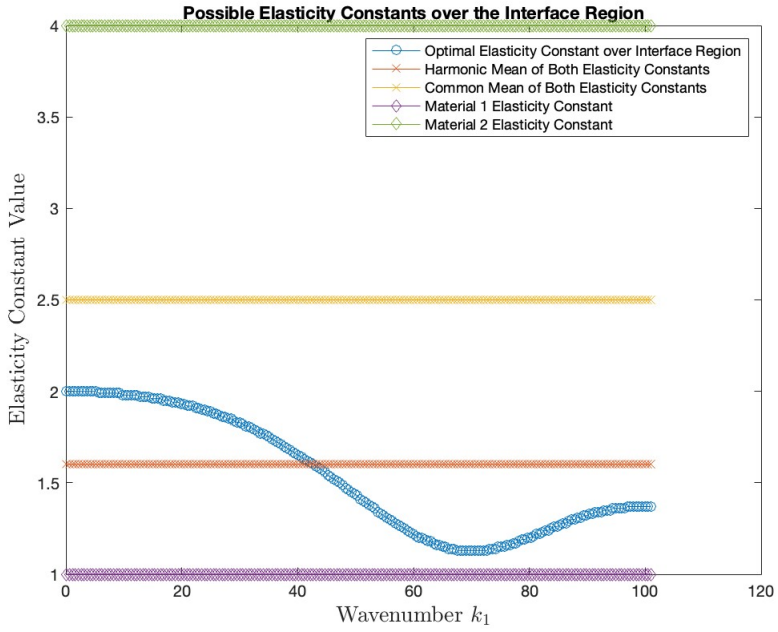

Figure 3.6: The value of the optimal cross-material property C_*, for $\gamma_* = \frac{C_*}{\delta^3}$, value found for each wave number k_1 that minimizes the nonlocal reflection. This is modeled against the values for the the interaction kernel values for each elasticity constant for the different materials and the harmonic mean and common mean values for comparison.

how this cross-material interaction term looks compared to the interaction term of each material, as well as the common mean and harmonic mean of each material's interaction term. The harmonic mean performs better than the common mean and would be suggested over the common mean.

CHAPTER 4: Future Work

Future work that extends from the Atomistic-to-Continuum chapter and the Peridynamics chapter will be discussed. I discuss more potential work for PD than for AtC as a result of my own interest in the applications of PD.

- **Extension of Blended Force-Based AtC Coupling to Two Dimensions** In the future, the extension of this scheme to two-dimensional atomistic-to-continuum coupling with a triangular crystal lattice with respect to the neighbors will be pursued. There are many types of defects that can occur in two-dimensional settings that are not exhibited in one-dimensional settings, such as impurities, vacancies, dislocations, and cracks, and there are still many open problems in two-dimensional problems for AtC coupling, including consistency and stability for many schemes [22]. The added difficulty with this extension is due to, but not limited to, the increased amount of neighbors, even if just looking at nearest and next-nearest neighbors because of the shape of the lattice. The increase in neighbors in this manner will add to the complexity of the numerical analysis, in addition to the efficiency of the computational scheme.

- **More Physically Relevant Values for the Bimaterial PD-PD Scheme** The work presented in this dissertation lays the foundation for further exploration of the dynamics of a one-dimensional PD-PD bimaterial system. The numerical analysis presented in this work will help design a structure-preserving numerical scheme that reduces numerical artifacts arising from interface reflections and preserves the conservation laws of this system. To further ad-

vance this research, several avenues can be pursued to enhance the physical validity of the system.

Horizon: One key extension involves considering different horizon values for the two materials, as opposed to the single horizon assumed between the two materials used in the current work. The choice in horizon value affects the complexity of the model and the nonlocal interaction kernels as they are currently defined in this work. Investigating the effects of dual horizons on the properties of the PD-PD system, such as energy flux and wave reflection, could provide valuable insight into the behavior of such systems in real-world scenarios.

Additionally, the function form and the size of the interface region over the material interface in terms of the interaction kernel function in the discrete setting warrant further investigation. Specifically, analyzing the stability of the numerical scheme in terms of the horizon size, similar to the stability analysis conducted for the blending size in the Atomistic-to-Continuum project in Chapter 2, could elucidate optimal parameter choices for the model.

Nonlocal Cross-Material Interaction Kernel:

Another important aspect to explore is the interaction kernel function itself. Although the current work employs a constant function for simplicity, using an interaction kernel that varies with the bond length between points or as a summation of basis functions could better reflect real-world conditions. Conducting dynamical stability analysis with respect to the smoothness of the kernel function could provide valuable insights into its influence on wave dispersion and the coefficient of reflection.

A similar extension of the interaction kernel function would be to utilize the ideas behind the smooth blending in Chapter 2 to the interface region (where

γ_* is employed). A smooth transition between the two materials could offer benefits over the sharp interface, as proposed in Chapter 3.

In summary, future work should focus on refining the numerical scheme to account for dual horizons, investigating the impact of the interaction kernel on system properties, and exploring more realistic forms of the interaction kernel function to enhance the physical relevance of the bimaterial PD-PD model.

- **Extension of Bi-Material PD-PD Scheme to Two Dimensions**

  Another next step in this research is to extend the bimaterial PD-PD scheme to two dimensions. However, this extension poses several challenges that need to be addressed.

  Firstly, the analysis becomes more complex because of the consideration of wave vectors and spatial vectors in two dimensions. This complexity adds difficulty to the analysis of conservation properties and introduces challenges in quantifying wave reflection.

  Moreover, the shape of the interface, the shape of the wave, and the direction of wave propagation in two dimensions further complicate the modeling process. These factors must be carefully considered to ensure the accuracy and reliability of the numerical scheme.

  We must also take into account how the size of the horizon affects the computational efficiency of a created scheme, especially as we move to two dimensions.

  The ultimate goal of this extension is to develop a numerical scheme for modeling the discretized two-dimensional PD-PD system that minimizes numerical artifacts, similar to the one-dimensional case. This scheme will be verified through extensive numerical simulations, which will provide validation

of the two-dimensional model and its applicability to real-world scenarios.

REFERENCES

[1] P. Seleson, S. Beneddine, and S. Prudhomme, "A force-based coupling scheme for peridynamics and classical elasticity," *Computational Materials Science*, vol. 66, pp. 34–49, 2013.

[2] I. Kondov and G. Sutmann, *Multiscale modeling methods for applications in materials science*. Forschungszentrum Julich, 2013.

[3] R. Miller and E. Tadmor, "A unified framework and performance benchmark of fourteen multiscale atomistic/continuum coupling methods," *Modelling and Simulation in Materials Science and Engineering*, vol. 17(5), p. 053001, 2009.

[4] E. Tadmor and R. Miller, *Modeling materials continuum, atomistic and multiscale techniques*. Cambridge University Press, first ed., 2011.

[5] W. E, *Principles of multiscale modeling*. Cambridge University Press, 2011.

[6] A. V. Shapeev, "Consistent energy-based atomistic/continuum coupling for two-body potentials in one and two dimensions," *SIAM J. Multiscale Model. Simul.*, vol. 9, no. 3, pp. 905–932, 2011.

[7] M. Luskin and C. Ortner, "Atomistic-to-continuum-coupling," *Acta Numerica*, vol. 22(4), pp. 397–508, 2013.

[8] S. Silling, "Reformulation of elasticity theory for discontinuities and long-range forces," *Journal of the Mechanics and Physics of Solids*, vol. 48, pp. 175–209, 2000.

[9] Q. Du, M. Gunzburger, R. Lehoucq, and K. Zhou, "Analysis and approximation of nonlocal diffusion problems with volume constraints," *SIAM Review*, vol. 56, pp. 676–696, 2012.

[10] P. Seleson, S. Beneddine, and S. Prudhomme, "A force based coupling scheme for peridynamics and classical elasticity," *Computational Materials Science*, vol. 66, pp. 34–49, 2013.

[11] P. Seleson, Y. D. Ha, and S. Beneddine, "Concurrent coupling of bond-based peridynamics and the Navier equation of classical elasticity by blending," *Journal for Multiscale Computational Engineering*, vol. 13, pp. 91–113, 2015.

[12] Q. Du and R. Lipton, "Peridynamics, fracture, and nonlocal continuum models," *SIAM News*, vol. 47, no. 3, 2014.

[13] M. D'Elia and M. Gunzburger, "Optimal distributed control of nonlocal steady diffusion problems," *SIAM Journal on Control and Optimization*, vol. 52, pp. 243–273, 2014.

[14] M. D'Elia, M. Perego, P. Bochev, and D. Littlewood, "A coupling strategy for nonlocal and local diffusion models with mixed volume constraints and boundary conditions," *Computers and Mathematics with applications*, vol. 71(11), pp. 2218–2230, 2015.

[15] K. Weinberg and A. Pandolfi, *Innovative numerical approaches for multi-field and multi-scale problems: in honor of Michael Ortiz's 60th birthday*. Springer, 2016.

[16] M. D'Elia, X. Li, P. Seleson, X. Tian, and Y. Yu, "A review of local-to-nonlocal coupling methods in nonlocal diffusion and nonlocal mechanics," *To appear on Journal of Peridynamics and Nonlocal Modeling*, 2020.

[17] N. Trask, H. You, Y. Yu, and M. L. Parks, "An asymptotically compatible meshfree quadrature rule for nonlocal problems with applications to peridynamics," *Computer Methods in Applied Mechanics and Engineering*, vol. 343, pp. 151–165, 2019.

[18] H. You, Y. Yu, and D. Kamensky, "An asymptotically compatible formulation for local-to-nonlocal coupling problems without overlapping regions," *Computer Methods in Applied Mechanics and Engineering*, vol. 366, 2020.

[19] M. Ortiz, "Multiscale modeling of materials – Michael Ortiz," 2013. www.youtube.com/watch?v=jM_7g4f7XlA.

[20] R. Phillips, *Crystals, defects and microstructures: modeling across scales*. Cambridge University Press, 2001.

[21] I. G. Graham, T. Y. Hou, O. Lakkis, and R. Scheichl, *Numerical analysis of multiscale problems*. Springer, 2012.

[22] M. Luskin and C. Ortner, "Atomistic-to-continuum coupling," *Acta Numerica*, vol. 22, pp. 397–508, 4 2013.

[23] R. B. Lehoucq and M. L. Parks, "Analysis of atomistic-to-continuum (atc) coupling methods.,"

[24] M. Luskin, C. Ortner, and B. Van Koten, "Formulation and optimization of the energy-based blended quasicontinuum method," *Computer Methods in Applied Mechanics and Engineering*, vol. 253, pp. 160–168, 2013.

[25] T. Shimokawa, J. J. Mortensen, J. Schiøtz, and K. W. Jacobsen, "Matching conditions in the quasicontinuum method: Removal of the error introduced at the interface between the coarse-grained and fully atomistic region," *Phys. Rev. B*, vol. 69, p. 214104, Jun 2004.

[26] W. E, J. Lu, and J. Z. Yang, "Uniform accuracy of the quasicontinuum method," *Phys. Rev. B*, vol. 74, p. 214115, Dec 2006.

[27] C. Ortner and L. Zhang, "Construction andx sharp consistency estimates for atomistic/continuum coupling methods with general interfaces: a 2D model problem," *SIAM Journal on Numerical Analysis*, vol. 50, 2012.

[28] X. Xu, M. D'Elia, and J. T. Foster, "A machine-learning framework for peridynamic material models with physical constraints," *Computer Methods in Applied Mechanics and Engineering*, vol. 386, p. 114062, 2021.

[29] C. T. Nguyen, S. Oterkus, and E. Oterkus, "A peridynamic-based machine learning model for one-dimensional and two-dimensional structures," *Continuum Mechanics and Thermodynamics*, vol. 35, no. 3, pp. 741–773, 2023.

[30] C. T. Nguyen, S. Oterkus, and E. Oterkus, "Chapter 20 - application of artificial intelligence and machine learning in peridynamics," in *Peridynamic Modeling, Numerical Techniques, and Applications* (E. Oterkus, S. Oterkus, and E. Madenci, eds.), Elsevier Series in Mechanics of Advanced Materials, pp. 419–435, Elsevier, 2021.

[31] E. Gorom-Alexander and X. H. Li, *A One-Dimensional Symmetric-Force-Based Blending Method for Atomistic-to-Continuum Coupling*, pp. 215–251. Cham: Springer International Publishing, 2023.

[32] X. Li, M. Luskin, and C. Ortner, "Positive definiteness of the blended force-based quasicontinuum method," *Multiscale Modeling & Simulation*, vol. 10, no. 3, pp. 1023–1045, 2012.

[33] T.-C. Lim *Zeitschrift für Naturforschung A*, vol. 58, no. 11, pp. 615–617, 2003.

[34] X. Li, M. Luskin, and C. Ortner, "Positive definiteness of the blended force-based quasicontinuum method," *Multiscale Modeling & Simulation*, vol. 10, no. 3, pp. 1023–1045, 2012.

[35] C. Ortner and A. Shapeev, "Analysis of an energy-based atomistic/continuum approximation of a vacancy in the 2d triangular lattice," *Mathematics of Computation*, vol. 82, no. 284, pp. 2191–2236, 2013.

[36] M. Dobson, C. Ortner, and A. V. Shapeev, "The spectrum of the force-based quasicontinuum operator for a homogeneous periodic chain," 2010.

[37] Y. D. Ha and F. Bobaru, "Studies of dynamic crack propagation and crack branching with peridynamics," *International Journal of Fracture*, vol. 162, pp. 229–244, 03 2010.

[38] A. Agwai, I. Guven, and E. Madenci, "Predicting crack propagation with peridynamics: a comparative study," *International Journal of Fracture*, vol. 171, no. 1, pp. 65–78, 2011.

[39] X. Zhou, Y. Wang, and Q. Qian, "Numerical simulation of crack curving and branching in brittle materials under dynamic loads using the extended non-ordinary state-based peridynamics," *European Journal of Mechanics - A/Solids*, vol. 60, pp. 277–299, 2016.

[40] M. D'Elia, D. J. Littlewood, J. Trageser, M. Perego, and P. B. Bochev, *An Optimization-Based Strategy for Peridynamic-FEM Coupling and for the Prescription of Nonlocal Boundary Conditions*, pp. 151–174. Cham: Springer International Publishing, 2023.

[41] S. Silling and R. Lehoucq, "Peridynamic theory of solid mechanics," in *Advances in Applied Mechanics* (H. Aref and E. van der Giessen, eds.), vol. 44 of *Advances in Applied Mechanics*, pp. 73–168, Elsevier, 2010.

[42] S. Kulkarni and A. Tabarraei, "An analytical study of wave propagation in a peridynamic bar with nonuniform discretization," *Engineering Fracture Mechanics*, vol. 190, pp. 347–366, 2018.

[43] G. Ongaro, P. Seleson, U. Galvanetto, T. Ni, and M. Zaccariotto, "Overall equilibrium in the coupling of peridynamics and classical continuum mechanics," *Computer Methods in Applied Mechanics and Engineering*, vol. 381, p. 113515, 2021.

[44] U. Galvanetto, T. Mudric, A. Shojaei, and M. Zaccariotto, "An effective way to couple fem meshes and peridynamics grids for the solution of static equilibrium problems," *Mechanics Research Communications*, vol. 76, pp. 41–47, 2016.

[45] W. Liu and J.-W. Hong, "A coupling approach of discretized peridynamics with finite element method," *Computer Methods in Applied Mechanics and Engineering*, vol. 245-246, pp. 163–175, 2012.

[46] S. Liu, G. Fang, J. Liang, and D. Lv, "A coupling model of xfem/peridynamics for 2d dynamic crack propagation and branching problems," *Theoretical and Applied Fracture Mechanics*, vol. 108, p. 102573, 2020.

[47] I. N. Giannakeas, T. K. Papathanasiou, A. S. Fallah, and H. Bahai, "Coupling xfem and peridynamics for brittle fracture simulation—part i: feasibility and effectiveness," *Computational Mechanics*, vol. 66, no. 1, pp. 103–122, 2020.

[48] X. Wang, S. S. Kulkarni, and A. Tabarraei, "Concurrent coupling of peridynamics and classical elasticity for elastodynamic problems," *Computer Methods in Applied Mechanics and Engineering*, vol. 344, pp. 251–275, 2019.

[49] S. A. Silling and R. B. Lehoucq, "Convergence of peridynamics to classical elasticity theory," *Journal of Elasticity*, vol. 93, no. 1, pp. 13–37, 2008.

[50] P. Seleson, M. L. Parks, M. Gunzburger, and R. B. Lehoucq, "Peridynamics as an upscaling of molecular dynamics," *Multiscale Modeling & Simulation*, vol. 8, no. 1, pp. 204–227, 2009.

[51] H. A. Nguyen, H. Wang, S. Tanaka, S. Oterkus, and E. Oterkus, "An in-depth investigation of bimaterial interface modeling using ordinary state-based peridynamics," *Journal of Peridynamics and Nonlocal Modeling*, vol. 4, no. 1, pp. 112–138, 2022.

[52] B. Kilic and E. Madenci, "An adaptive dynamic relaxation method for quasi-static simulations using the peridynamic theory," *Theoretical and Applied Fracture Mechanics*, vol. 53, no. 3, pp. 194–204, 2010.

[53] D. Behera, P. Roy, and E. Madenci, "Peridynamic modeling of bonded-lap joints with viscoelastic adhesives in the presence of finite deformation," *Computer Methods in Applied Mechanics and Engineering*, vol. 374, p. 113584, 2021.

[54] S. Oterkus, E. Madenci, and A. Agwai, "Peridynamic thermal diffusion," *Journal of Computational Physics*, vol. 265, pp. 71–96, 2014.

[55] F. Wang, L. Liu, Q. Liu, Z. Zhang, L. Su, and D. Xue, "Studies of bimaterial interface fracture with peridynamics," 01 2015.

[56] H. Zhang, X. Zhang, Y. Liu, and P. Qiao, "Peridynamic modeling of elastic bimaterial interface fracture," *Computer Methods in Applied Mechanics and Engineering*, vol. 390, p. 114458, 2022.

[57] P. H. G. S. A. S. Florin Bobaru, John T. Foster, ed., *Handbook of Peridynamic Modeling*. Chapman and Hall/CRC, 1st ed., 2016.

APPENDIX A: A More Rigorous Proof for Proposition 2.2.2, A Consistency Analysis of Force

Proof. Comparing $F^{c,lin}$ and $F^{a,lin}$, we have the following

$$F^{c,lin}_{\ell,}(u) - F^{a,lin}_{\ell,}(u) = -\sum_{\substack{k=-N,\\ k\neq 0}}^{N} \frac{1}{2}\phi_{xx}(k)\left(k^2 u''_\ell\right) + \sum_{\substack{k=-N,\\ k\neq 0}}^{N} \frac{1}{2}\phi_{xx}(k)\left(\frac{u_{\ell+k} - 2u_\ell + u_{\ell-k}}{a^2}\right).$$

Let $N \in \mathbb{N}$ be fixed. For any $k = -N, \ldots, N$ and $k \neq 0$, we apply the Taylor expansion to $\widetilde{u}_{\ell+k} = u_{\ell+k}$ and $\widetilde{u}_{\ell-k} = u_{\ell-k}$ around ℓ. We compare the differencing notation used to define the discrete displacement field with choosing a smooth spline interpolation. We proceed by defining $\widetilde{u}_x$ as this smooth interpolation of the discrete displacement field u in order to compute this approximation.

$$\begin{aligned} u_{\ell+k} &= u_\ell + ka\widetilde{u}_x + \frac{1}{2}(ka)^2\widetilde{u}_{xx} + \frac{1}{6}(ka)^3\widetilde{u}_{xxx} + O(a^4), \\ u_{\ell-k} &= u_\ell - ka\widetilde{u}_x + \frac{1}{2}(ka)^2\widetilde{u}_{xx} - \frac{1}{6}(ka)^3\widetilde{u}_{xxx} + O(a^4). \end{aligned}$$

Thus, for all k,

$$\begin{aligned} u_{\ell+k} - 2u_\ell + u_{\ell-k} &= u_\ell + ka\widetilde{u}_x + \frac{1}{2}(ka)^2\widetilde{u}_{xx} + \frac{1}{6}(ka)^3\widetilde{u}_{xxx} + O(a^4) - 2u_\ell \\ &\quad + u_\ell - ka\widetilde{u}_x + \frac{1}{2}(ka)^2\widetilde{u}_{xx} - \frac{1}{6}(ka)^3\widetilde{u}_{xxx} + O(a^4) \\ &= (ka)^2\widetilde{u}_{xx} + O(a^4). \end{aligned} \tag{A.0.1}$$

Utilizing (A.0.1) for the atomistic and continuous force equations, the consistency

analysis yields:

$$
\begin{aligned}
&F_{\ell,}^{c,lin}(u) - F_{\ell,}^{a,lin}(u) \\
&\quad = -\sum_{\substack{k=-N,\\ k\neq 0}}^{N} \frac{1}{2}\phi_{xx}(k)\left(k^2 u_\ell''\right) + \sum_{\substack{k=-N,\\ k\neq 0}}^{N} \frac{1}{2}\phi_{xx}(k)\left(\frac{u_{\ell+k} - 2u_\ell + u_{\ell-k}}{a^2}\right) \\
&\quad = -\sum_{\substack{k=-N,\\ k\neq 0}}^{N} \frac{1}{2}k^2\phi_{xx}(k)\left(\frac{u_{\ell+1} - 2u_\ell + u_{\ell-1}}{a^2}\right) \\
&\qquad + \sum_{\substack{k=-N,\\ k\neq 0}}^{N} \frac{1}{2}\phi_{xx}(k)\left(\frac{u_{\ell+k} - 2u_\ell + u_{\ell-k}}{a^2}\right) \\
&\quad = -\sum_{\substack{k=-N,\\ k\neq 0}}^{N} \frac{1}{2}k^2\phi_{xx}(k)\frac{a^2\widetilde{u}_{xx} + O(a^4)}{a^2} + \sum_{\substack{k=-N,\\ k\neq 0}}^{N} \frac{1}{2}k^2\phi_{xx}(k)\frac{(ka)^2\widetilde{u}_{xx} + O(a^4)}{a^2} \\
&\quad = -\sum_{\substack{k=-N,\\ k\neq 0}}^{N} \frac{1}{2}k^2\phi_{xx}(k)\widetilde{u}_{xx} + \sum_{\substack{k=-N,\\ k\neq 0}}^{N} \frac{1}{2}k^2\phi_{xx}(k)\widetilde{u}_{xx} + O(a^2) \\
&\quad = O(a^2).
\end{aligned}
$$

Thus, the consistency error between the linearized atomistic force equation and the continuum force equation is $O(a^2)$. □

APPENDIX B: Analysis in the continuous setting

Before finding the nearest-neighbor and the next-nearest-neighbor interaction for the discrete case, the continuous case was observed. The continuous case was meant to shed light on the nature of the discrete case as it would be easier to find.

From (2.2.17) we look at the next-nearest neighbor interaction. Also, we will approximate $\frac{\beta_{\ell+k}+2\beta_\ell+\beta_{\ell-k}}{4} \approx \beta(x_\ell)$. Thus, (2.2.17) becomes for the force-based operator:

$$\begin{aligned}
F_{\ell,}^{bqcf,lin} &= \left(\frac{\beta_{\ell-1}+2\beta_\ell+\beta_{\ell+1}}{4}\right)\phi_{xx}(1)\left(\frac{u_{\ell+1}-2u_\ell+u_{\ell-1}}{a^2}\right) \\
&+ \left(1-\frac{\beta_{\ell-1}+2\beta_\ell+\beta_{\ell+1}}{4}\right)\phi_{xx}(1)u_\ell'' \\
&+ \left(\frac{\beta_{\ell-2}+2\beta_\ell+\beta_{\ell+2}}{4}\right)\phi_{xx}(2)\left(\frac{u_{\ell+2}-2u_\ell+u_{\ell-2}}{a^2}\right) \\
&+ \left(1-\frac{\beta_{\ell-2}+2\beta_\ell+\beta_{\ell+2}}{4}\right)\phi_{xx}(2)4u_\ell'' \\
&\approx \beta(x_\ell)\left(\phi_{xx}(1)u_\ell'' + \phi_{xx}(2)\left(\frac{u_{\ell+2}-2u_\ell+u_{\ell-2}}{a^2}\right)\right) \\
&+ \left(1-\beta(x_\ell)\right)\left(\phi_{xx}(1)u_\ell'' + 4\phi_{xx}(2)u_\ell''\right).
\end{aligned}$$

Using a Taylor approximation on $u_{\ell+2}$ and $u_{\ell-2}$, the next-nearest neighbor operator becomes

$$F_{\ell,}^{bqcf,lin} = \phi_{xx}(1)u_\ell'' + \beta(x_\ell)\phi_{xx}(2)\left(4u_\ell'' + \frac{4}{3}u_\ell^{(4)}a^2\right) + \left(1-\beta(x_\ell)\right)4\phi_{xx}(2)u_\ell''. \tag{B.0.1}$$

Since the nearest neighbor interaction is not difficult to find, we drop it from the continuous case to find the approximation for the next-nearest neighbor as well as utilize the fact that ϕ is a Lennard-Jones type potential. Also, we denote $\beta(x_\ell)$ by β when there is no ambiguity. Therefore, the continuous next-nearest operator

becomes

$$\begin{aligned} Fu_x &= \beta(-u_{xx} + a^2 A u_{xxxx}) + (1-\beta)(-u_{xx}) \\ &= \beta a^2 A u_{xxxx} - u_{xx} \end{aligned} \tag{B.0.2}$$

where $A = \frac{4}{3}$.

Lemma B.0.1. *For any displacements $u = (u_\ell)_{\ell\in\mathbb{Z}}$ from y_ℓ, the nearest neighbor and the next-nearest neighbor interaction operator can be written in the form*

$$\begin{aligned} &< F_{,1}^{bqcf,lin}, u >= \|u_x\|^2 \\ &< F_{,2}^{bqcf,lin}, u >= 4\|u_x\|^2 + a^2 16A\left\|\sqrt{\beta}u_{xx}\right\|^2 + R + S. \end{aligned} \tag{B.0.3}$$

where R and S are given by:

$$R = -a^2 A\int \beta_{xx}(u_x)^2 dx, \quad S = a^2 A\int \beta_{xx}(u_{xx}u)dx. \tag{B.0.4}$$

Proof. Since the proof of the first identity of Lemma B.0.1 is straightforward and utilizes the same properties, the proof for the second-neighbor interaction operator will be given. The main tool used is integration by parts based on the periodic boundary conditions.

$$\begin{aligned} < F_{,2}^{bqcf}u, u > &= \int(\beta a^2 B u_{xxxx} - u_{xx})u dx \\ &= \int -u_{xx}u dx + \int \beta a^2 A u_{xxxx} u dx \\ &= \int (u_x)^2 dx + a^2 A\int \beta u u_{xxxx} dx \\ &= \|u_x\|^2 - a^2 A\int(\beta u)_x u_{xxx} dx \\ &= \|u_x\|^2 + a^2 A\left\|\sqrt{\beta}u_{xx}\right\|^2 + a^2 A\int \beta_x (u_x)_x^2 dx - a^2 A\int \beta_x (u\, u_{xx})_x dx \end{aligned}$$

$$< F_{,2}^{bqcf} u, u > = \|u_x\|^2 + a^2 A \left\| \sqrt{\beta} u_{xx} \right\|^2 - a^2 A \int \beta_{xx} (u_x)^2 dx + a^2 A \int \beta_{xx} (u_{xx} u) dx$$
$$= \|u_x\|^2 + a^2 A \left\| \sqrt{\beta} u_{xx} \right\|^2 + R + S. \tag{B.0.5}$$

Using the continuous analysis as a road map, we thus derive the discrete analysis in Section 3. □